2003

Structure of alkali tungsten tellurite glasses by X-ray photoelectron spectroscopy and LiNbO3 based transparent, nano-composite, glass ceramics

Jong Wook (Austin) Lim
Lehigh University

Lim, Jong Wook (Austin)

Structure of Alkali Tungsten Tellurite Glasses by X-Ray Photoelectron Spectroscopy and LiNbO3 Based...

January 2004

Structure of alkali tungsten tellurite glasses by X-ray photoelectron spectroscopy

and

$LiNbO_3$ based transparent, nano-composite, glass-ceramics

by

Jong Wook (Austin) Lim

A Thesis

Presented to the Graduate and Research Committee

of Lehigh University

in candidacy for the Degree of

Master of Science

in

Materials Science and Engineering

Lehigh University

December 2003

This Thesis is accepted and approved in partial fulfillment of the requirements for the Master of Science Degree.

Sept 24, 2003

Date

Himanshu Jain
Thesis Advisor

G. Slade Cargill III
Chairperson of Department

Acknowledgements

I would like to express my gratitude to my advisor, Dr. Himanshu Jain, for his support and guidance. I am especially grateful that he did not give up on me when I had difficult time concentrating on the work during first year of graduate school. I have received and benefited from his knowledge and understanding of glass science.

I thank my other advisor, Dr. Jean Toulouse, with whom I had many fruitful discussions and who provided me guidance for my research. I express my thank to Dr. Jas Sanghera, Naval Research Laboratory, for providing tellurite glass samples for my research as well as for his suggestions. I also thank our collaborators, Dr. Venkat Gopalan and Dr. Alok Sharan, Pennsylvania State University, who researched SHG measurement for me.

I would like to thank our professors in Department of Materials Science and Engineering for the great educational experience that I had. I also express my thanks to David Ackland, Arlan Benscoter, Gene Kozma for their help and sharing experience in electron microscopy, polishing samples, and fixing furnace respectively. I thank the department staff, Maxine Mattie, Deanne Hoenscheid, Virginia Newhard for support during my stay.

I especially acknowledge the help of and discussions with Dr. Alfred C. Miller on the X-ray Photoelectron Spectroscopy experiments that were performed during the course of this work.

I would like to thank my family and my friends, especially my parents, for their love, understanding, patience and trust. I express my special thanks to my fiancé, Hye Hyun Park for her constant love, encouragement, and support of my studies. Their love and trust have encouraged me to accomplish my goal.

I am grateful to all members of my research group and other graduate students, Fasial Alamgir, Gang Chen, Pradyumna Gupta, Keisha Antoine, David Laughman, Sumi Krishnaswami, Adam Scotch, Paul Sheedy, Edward Gorzkowski, Patrick King, and Derrick Rockosi; and post-doc/visiting scientists: Hyung Jun Park, Seung Min Hyun, Masashi Watanabe, and Christian Trquat who have helped me in one way or the other.

I would also like to thank the National Science Foundation for financial support under grant No. DMR9974031.

Table of Contents

List of Tables

List of Figures:

Abstract

This thesis is a result of two research projects both of which focus on the structure of glassy optical materials. In the first project, the electronic structure of two alkali tungsten tellurite glass series: (a) $10Li_2O$ *xWO_3*$(90-x)TeO_2$, (b) xK_2O*$(10-x)Li_2O$ *$25WO_3$*$65TeO_2$ has been investigated by X-ray photoelectron spectroscopy. The samples were fractured *in situ* under high vacuum conditions before observing the spectra with excitation by monochromatic Al Kα X-rays. In contrast to binary alkali tellurite glasses, the core level spectra of the various elements appear unaffected when TeO_2 is replaced by WO_3, with the alkali oxide concentration remaining constant. The O 1s spectra do not indicate a clear separation of the bridging and non-bridging oxygen contributions. Thus we conclude that WO_3 behaves essentially as a network former in tellurite glasses. We have also obtained valence band spectra of the various series and found major changes with the addition of WO_3. In particular, the lowest energy part of these spectra, attributed to the O 2p bonding orbital, decreases significantly with increasing WO_3, indicating the appearance of a new bonding configuration.

In the second project, the transparent ferroelectric glass-ceramic nano-composites containing $LiNbO_3$ were synthesized and their structure was investigated. A series of x $(Li_2O*2SiO_2)$ * $(1-x)(Li_2O*Nb_2O_5)$ glasses was prepared by the melt quench method with x = 0.3 – 0.9. The glass formation range x $(Li_2O*2SiO_2)$ * $(1-x)(Li_2O*Nb_2O_5)$ pseudo binary system was established for within x = 0.4 – 0.9. The amorphous structure

of these optically transparent glasses at low silica was established and characterized by X-ray diffraction, scanning electron microscope, and transmission electron microscopy (TEM). By appropriate heat treatment and thermal poling, the glasses were partly crystallized to precipitate nano-crystallites of $LiNbO_3$. The glass transition temperature, glass-ceramic formation, and second harmonic optical properties were determined as a function of x.

Chapter 1 Introduction

Typically, transparent glasses are used in windows, light bulbs, laboratory ware, and so on. However, with the development of optical fiber telecommunication, glass is proven as a key optical material for photonic technology. The low cost optical silica glass is responsible for the photonic revolution of present days. It is used in optical fibers which are able to transmit very dense information in the form of short optical light pulses over hundreds of kilometers. Optical fibers in use today operate near the theoretical minimum absorption value of 0.15 dB/km[1]. Since the time the glass is found as an ideal medium for the transmission of light, its many more potential uses have been recognized in optical communication.

Even though silica glass is widely used as the most transparent optical glass fiber, there are many other glasses with different physical and chemical properties that have potential for additional photonic applications at lower cost. For example, tellurite glasses and glass-ceramics can be synthesized as inexpensive optical materials with higher linear and nonlinear refractive indices. The purpose of this work is to study the electronic structure of tellurite glasses, which is the basis of their superior optical properties. In addition, transparent glass-ceramics are prepared with nonlinear optical properties.

In general, tellurite glasses are one of the most promising candidate materials for optical applications. They are characterized by high refractive index (larger than 2.0), wide band infrared transmittance (extending up to 6000 nm), and large third order non-linear optical susceptibility [2, 3]. In addition, tellurite glasses combine the attributes of a

short wavelength UV edge (about 350 nm), good glass stability, rare earth ion solubility, a slow corrosion rate, and relatively low phonon energy among oxide glass formers[4]. Tellurite glasses are capable of providing a large stimulated emission cross section over a broad bandwidth. Furthermore, the phonon energy of tellurite glasses is about 600 cm^{-1} to 850 cm^{-1} [4].

The fascinating properties of tellurite glass are due to its anomalous network and electronic structure. However, definite picture of their structure has not been obtained. In the past, several research groups have investigated the network and electronic structures of tellurite glasses for several years by using different experimental methods. For example, binary tellurite glasses containing alkali oxides[5-9] have been studied by infrared[5-8], Raman[5, 7-9], and X-ray photoelectron spectroscopies [5]. Our study has focused on the structural development of alkali tellurite glasses within the Li_2O- WO_3 - TeO_2 ternary system. In order to investigate the electronic structure we have used X-ray photoelectron spectroscopy.

Glass-ceramics are polycrystalline materials formed by the controlled crystallization of glass. Transparent glass-ceramics may be prepared to combine the advantages of glass (e.g., easy to fabricate as fiber or waveguides) and unique properties of crystal phase (e.g., electro-optical properties) in the same material. Obviously, their transparency depends on crystal size and birefringence, and of the difference in refractive index of the crystals and the host glass[10]. These glass-ceramics may exhibit strong non-linear response ferroelectric properties. However, the structure of the glass-ceramics needs to be controlled precisely such that the emerging crystallites are large enough to

show ferroelectric properties, but small enough to remain transparent to light. The optimum size is anticipated to be in the range of several 10s of nanometers[10].

Ferroelectric materials such as niobates, titanates and tantalates have become very important in optical communication systems. These crystals permit electrical control of linear and nonlinear optical properties. However, such crystals have disadvantages that they are expensive and difficult to fabricate. Therefore, we have tried to prepare transparent ferroelectric glass-ceramics, which have large nonlinear optical properties at a much lower cost.

To study transparent ferroelectric nano-composite (TFN) glass-ceramics, lithium niobium silicate glasses have been investigated[17-19]. Lithium niobate, $LiNbO_3$, is the most commonly used optical ferroelectric material with a curie temperature of 1210 °C. It is an efficient non-linear optical material for second harmonic generation and is widely used for optical waveguides[11]. Silicate glasses are cheap and have superior physical properties. Previous researches have studied potassium[12, 13] and sodium niobium silicate glass-ceramics and they found nonlinear response in these materials[14-16]. Lithium niobium silicate glass-ceramics have been also studied[17-19] but in this case second harmonic generation (SHG) originated only from the surface crystallized layers. Naturally, the effect / volume has been relatively small. So, the aim of this work is to obtain transparent glass-ceramics with ferroelectric nonlinear optical properties not only on the surface but also in the bulk. A correlation is sought between the processing, microstructure and nonlinear properties of these TFNs.

Chapter 2 Background

2.1 Tellurite glass structure

Nonetheless, Pure TeO_2 cannot be made easily into a glass using conventional melting methods, except under special conditions involving the addition of impurity elements. The understanding of the local structure of alkali tungsten tellurite glasses is based on the structure of pure TeO_2 glass. There are two crystalline forms of TeO_2: α-TeO_2 which consists of a network of interconnected TeO_4 trigonal bipyramids with equatorial ($Te\text{-}O_{eq}$) and axial ($Te\text{-}O_{ax}$) bond lengths equal to 1.90 and 2.08 Å, respectively (Figure 2.1 (a)) [20, 21]. There is also a lone pair of electrons in the third equatorial position. On the other hand, β-TeO_2 consists of an interconnected network of $(Te_2O_6)^{4-}$ units that can be thought of as two trigonal bipyramids that share an edge, each with an equatorial lone pair of electrons (Figure. 2.1 (b)) [22]. One of the axial Te-O bonds of the bipyramid is slightly longer (2.19Å) than the other three (averages 1.96Å) [23]. Recently, Suehare et al. [20, 21] calculated the electronic structure of pure TeO_2 glass by the self-consistent charge discrete-variational Xα (SCC-DV- Xα) method. The calculated valence band spectrum is in good agreement with the experimental spectrum for α-TeO_2 single crystal. As regards these results, the electronic states of pure TeO_2 glass and α-TeO_2 single crystal are similar to each other. This means that the pure TeO_2 glass and α-TeO_2 crystal have the same basic structural unit: TeO_4 trigonal bipyramids (tbp).

Several research groups have investigated the atomic and electronic structure of tellurite glasses for several years using different experimental methods. For example, binary tellurite glasses containing alkali oxides [5-9] have been studied by infrared [5-8], Raman and X-ray photoelectron spectroscopies [5, 7-9]. Structural models are developed based on two oxygen coordination numbers (3 and 4) for the Te (+IV) atoms. Himei et al. [25] studied X-ray photoelectron spectroscopy of alkali tellurite glasses and found that there is only one component in the O 1s peak. According to previous studies, all oxygen atoms ($Te\text{-}_{ax}O_{eq}\text{-}Te$) occur as bridging oxygen (BO) in the pure tellurite glass. One might expect that the addition of a modifier oxide as in silica would break up the three-dimensional network of pure TeO_2 glass with the formation of singly or double bonded non-bridging oxygen (NBO). NBO with a single bond has one negative formal charge (O^-), which is neutralized by the positively charged modifier ion (M^+) around it [26]. However, Himei group did not observe two peaks, which could be attributed to BO and NBO, respectively.

For the possible change of coordination number of tellurium atoms with the addition of alkali oxides, Neov *et la.*[27] suggested that some of the oxygen ions of modifiers present in specific structure regions may satisfy the coordination polyhedron to form a trigonal bipyramid in the equatorial position. Then, some of the axial bonds break off the chain structure and form a new fourfold coordinated tellurium, having three oxygen atoms in equatorial and one in the axial position. In addition to their model, Sekiya *et al.* [26] proposed and later Moawad et al.[47] confirmed that NBOs are created by the addition of alkali oxide modifier into TeO_2 network. The NBOs have a negative

charge associated with them and TeO_4 trigonal bipyramids (tbp) are deformed into lower-symmetry TeO_{3+1} polyhedra. TeO_3 trigonal pyramids (tp) start to appear when the amount of alkali increases beyond 20 to 30 moles %, where the NBO is linked to the tellurium by a double bond. Their model is shown in Figure 2.2. Thus, most recent studies have concluded that TeO_4 trigonal bipyramids (tbp) change to TeO_3 trigonal pyramids (tp) through TeO_{3+1} polyhedra and one of their equatorial positions is occupied by a lone pair of electron in the glass structure.

Some groups have studied binary tellurite glass system other than the alkali tellurite glasses. Tellurite tungstate (TeO_2-WO_3) are super heavy flint glasses which show refraction index, $n > 2.0$ and a low dispersion value of $\upsilon \sim 18$ [28]. The structure of these glasses has been investigated by infrared spectroscopy, X-ray and neutron diffraction, and Raman spectroscopy [29-31]. Dimitrov et al. [29] argued that a part of TeO_2 is replaced by WO_4 tetrahedra and the coordination state of a fraction of tungsten atoms changes from WO_4 tetrahedron to WO_6 octahedron with increasing WO_3 content. However, Sekiya et al. [26] disagreed with Dimitrov's conclusion and they suggested creation of WO_6 octahedra even with the initial addition of WO_3. From Raman spectra, they found that on adding WO_3, Te-O-Te units are replaced by W-O-W and the W-O-Te units. In the entire composition range of these glasses, W=O bonds are present. Accordingly, WO_6 having W=O bonds is in six coordination not four coordination, and this octahedra shares corners. In addition, the WO_6 octahedra having W=O bonds share some of the remaining vertices with TeO_{3+1} polyhedra forming $Te\text{-}_{short}O\text{-}W$ linkages [26].

2.2 Ferroelectric Glass-ceramics

2.2.1 Glass-ceramics

As we mentioned earlier, glass-ceramics are polycrystalline materials formed by the controlled crystallization of glass. Most glass-ceramics are developed by glass forming processes and converted to a crystalline product by proper heat treatment. The range of glass ceramic composition can be broad, but the given composition should have the ability to form glass and then be amenable to controlled crystallization.

Glass-ceramics provide several advantages over glass or ceramic materials. They are easy to fabricate in complex forms and at the same time possess superior properties. They posses highly uniform microstructure with grain size on the order of 10 micrometers or less. This homogeneity ensures that their physical properties are highly reproducible. Glassmakers have traditionally aimed to formulate highly stable glass compositions that are resistant to devitrification in order to minimize the crystal growth rate in the working range. However, it was reasoned that careful controlled crystallization might provide glass with greatly improved mechanical properties. Since the principles of nucleation and growth have been developed, glass-ceramics technology has led to the production of a range of materials including transparent, zero expansion materials with excellent optical properties to jade-like highly crystalline materials with excellent strength and toughness.[10]

To develop glass-ceramics, the nucleation and crystallization states are very important, because they determine the ultimate microstructure. The desired crystallite

size depends on the temperature and time of heat treatment. For the bulk glass-ceramic processing, the materials are melted and fabricated in the glassy state. Next the glass is crystallized using a heat treatment designed for that material. Typically, this process consists of a low temperature hold to induce nucleation, followed by higher temperature annealing to promote crystallization and to grow the primary phase (Figure 2.3). Nucleation is a decisive factor for controlled crystallization as it initiates the development of crystals in the base glass. Submicroscopic crystalline nuclei precipitate on heating to temperatures about 30~100 °C above the annealing point of the host glass. Even though useful properties do not appear at this stage, these nuclei serve as the sites for subsequent growth of the primary crystalline phases. The growth of crystallites leads to the development of the desired microstructure. During this stage of the heat treatment, the primary crystalline phases grow gradually until they impinge on neighboring crystallites. At the early stages, the primary crystallite sizes are nano-sizes and these glass-ceramics that have nano-crystallite are still transparent.

The degree of transparency of a glass-ceramic is a function of crystal size, birefringence (if any), and the difference in refractive index between the crystals and the residual glass [32, 33]. When the crystals are much smaller than ($\lambda < \sim 390$ nm the limit of the visible region) the wavelength of light or when the crystals have low birefringence and the index of refraction is closely matched, excellent transparency can be achieved. Certain glass-ceramic materials also exhibit potentially useful electro-optic effects. These include glasses with microcrystallines of Cd-sulfoselenides, which show a strong nonlinear response to an electric field [34]. In addition, there are glass-ceramics based on

ferroelectric perovskite crystallites such as niobates, titanates, or zirconates [35-37]. These materials can be used in a number of electro-optics applications.

The materials selected for our studies are ferroelectric glass-ceramic nano-composites. They are initially formed as glasses that contain potentially ferroelectric component and glass forming oxide such as SiO_2. Some groups have previously studied; silica based TFNs, viz. $25Li_2O*25Nb_2O_5*50SiO_2$ [17], $45Li_2O*20Nb_2O_5*35SiO_2$ [18], $35Li_2O*30Nb_2O_5*35SiO_2$ [19] (Figure 2.4). They prepared transparent glass-ceramics containing $LiNbO_3$ crystallites by controlling heat treatment and their nano-composite glass-ceramic showed optical nonlinearity. However $LiNbO_3$ nano-crystallites were present only on the surface of samples and not in the bulk.

2.2.2 Ferroelectrics and poled glasses

Ferroelectric oxides are some of the most important materials for photonic technology based on their nonlinear behavior, especially, in their optical properties. They develop electric dipoles spontaneously in their crystal structure as illustrated in Figure 2.5 for the case of $LiNbO_3$. When light with electric field **E** is applied to a ferroelectric nonlinear optical material, its response can be described by the polarization vector P which shows how the electrons/ions oscillate in the presence of the electromagnetic wave. The charge oscillation is responsible for the propagation of light in the medium and the result of structural anisotropy provides nonlinear optical properties such as electro optic effect (change in optical index with electric fields), harmonic generation

(changing frequency of light), and so on. The nonlinear polarization can be described in terms of a power series of the electric field given by,

$$P_i = \varepsilon_0 \chi_{ij} E_j + \varepsilon_0 \chi_{ijk} E_j E_k + \varepsilon_0 \chi_{ijkl} E_j E_k E_l + ...$$

where ε_0 is the vacuum permittivity and χ is dielectric susceptibility tensor elements of various orders and E is a component of electric field; subscripts i, j, k, l etc. specify the crystal coordinate axes. χ_{ij} is the linear susceptibility, which is related both to the absorption of the material (imaginary part) and to its refractive index (real part). The second order nonlinear susceptibility describes the second order nonlinear effects such as frequency doubling (second harmonic generation), sum and difference frequency generation, the electro optical effect, and optical rectification. The larger the value of χ_{ijk}, the greater the effect becomes. A material with large χ_{ijk} subjected to an intense optical field E_ω has polarization with a cross term $E_\omega E_\omega$ that oscillates with angular frequency 2ω that is capable of frequency doubling the input radiation [24]. For example, SHG (second harmonic generation) is present in the output as a weak, green coherent radiation component at 532nm, half the wavelength of the incoming light at 1064 nm. A material with a large second order optical nonlinearity can be used for the modulation of light.

Actually, glass has macroscopic inversion symmetry. The symmetric distortion of the potential does not give rise to a second order nonlinearity (SON) and χ_{ijk} is zero.

Therefore, efficient SHG and the linear electro-optical effect are generally not expected in glass systems. However, it was observed by Myers *et al.* [38] that a permanent and large SON could be generated in fused silica using thermal poling. The poled sample was illuminated with a strong infrared (ir) laser beam. They discovered that it was the silica glass that was generating the green light and they had induced a strong optical nonlinearity in silica by thermal poling. In addition, there are some studies that have reported the nonlinear optical properties of ferroelectric glass nanocomposites. The second harmonic generation response has been found in glass composites within the Li_2O-Nb_2O_5-TeO_2 [39], $LaBGeO_5$ [40], $BaTiO_3$-SiO_2 [41] and K_2O-Nb_2O_5-SiO_2 [13, 42] systems. These reports have mentioned the feasibility of forming transparent ferroelectric glass nanocomposites and shown that they possess useful nonlinear optical properties.

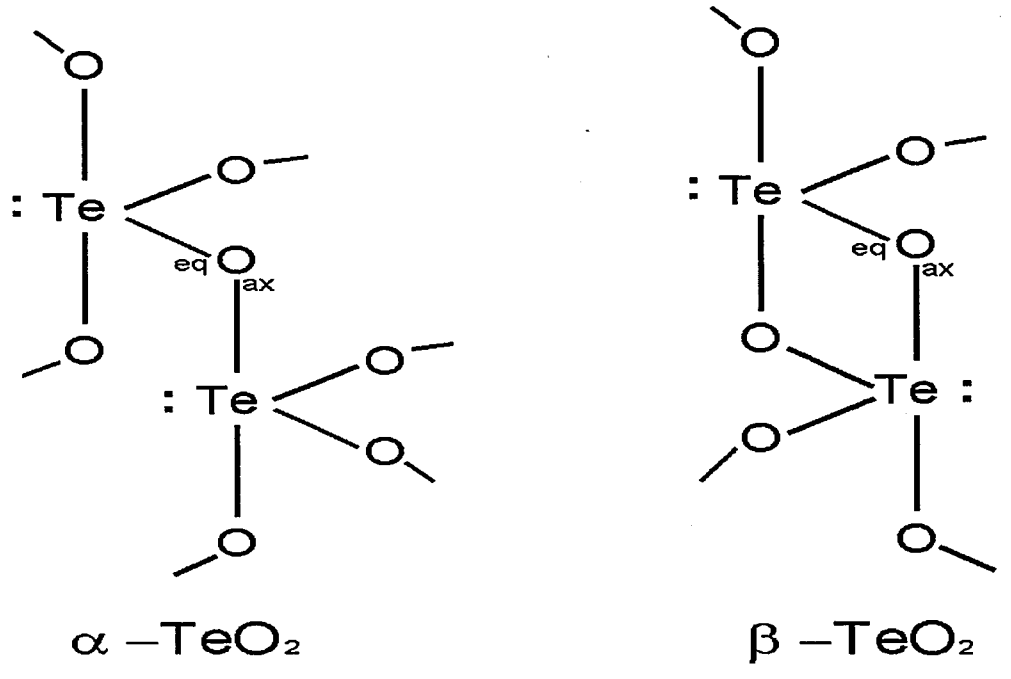

Figure 2.1. Illustration of pure TeO_2 (a) α-TeO_2, (b) β-TeO_2

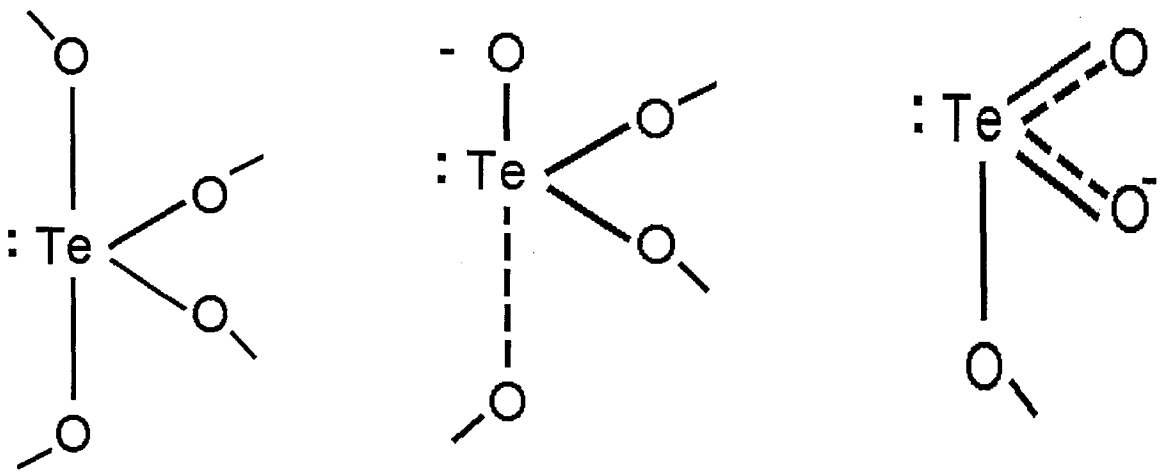

Figure 2.2. Illustration of the tellurium atom coordination by oxygen:

(a) TeO_4 trigonal bipyramid (tbp).

(b) TeO_{3+1}^- polyhedron.

(c) TeO_3 trigonal pyramid (tp).

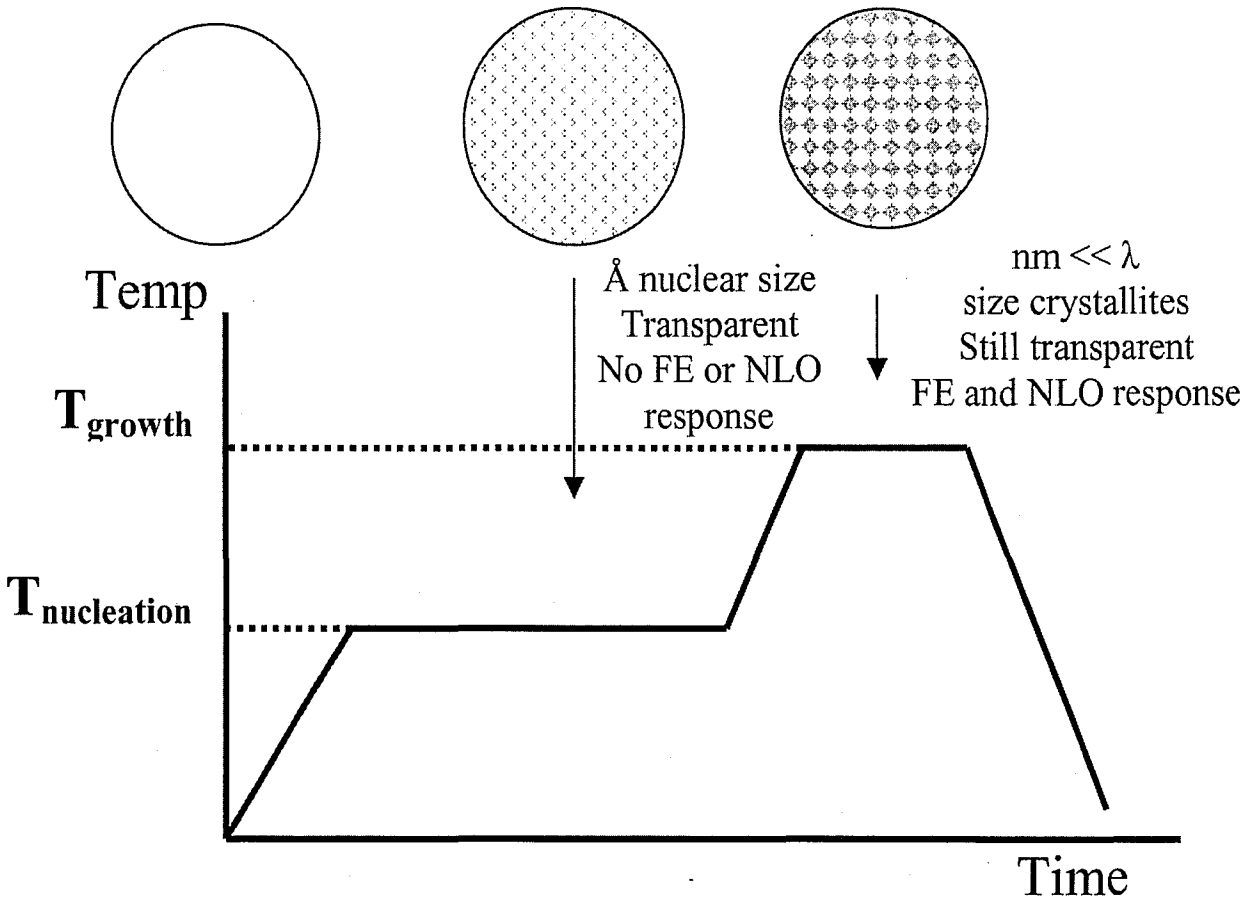

Figure 2.3. Heat treatment cycle for a glass-ceramic material.

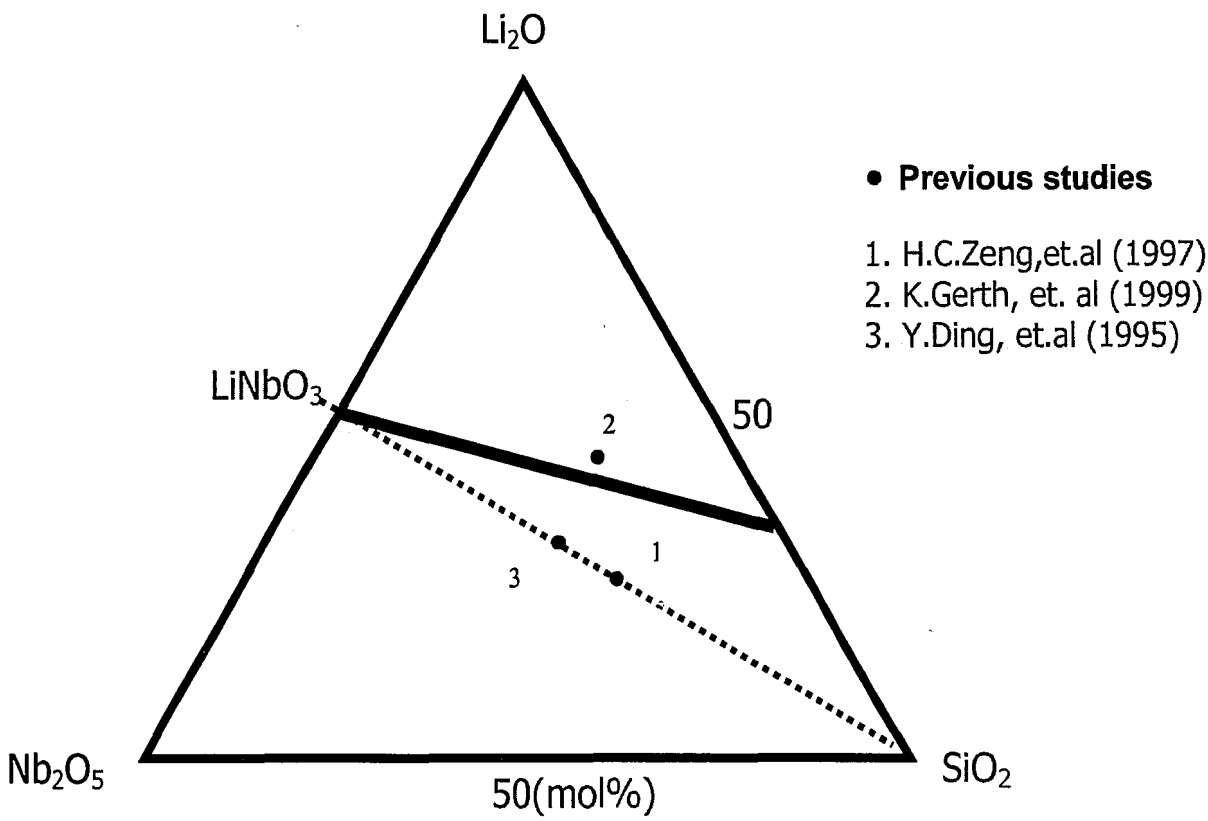

Figure 2.4. Diagram for previous studies of Li_2O-Nb_2O_5-SiO_2 system

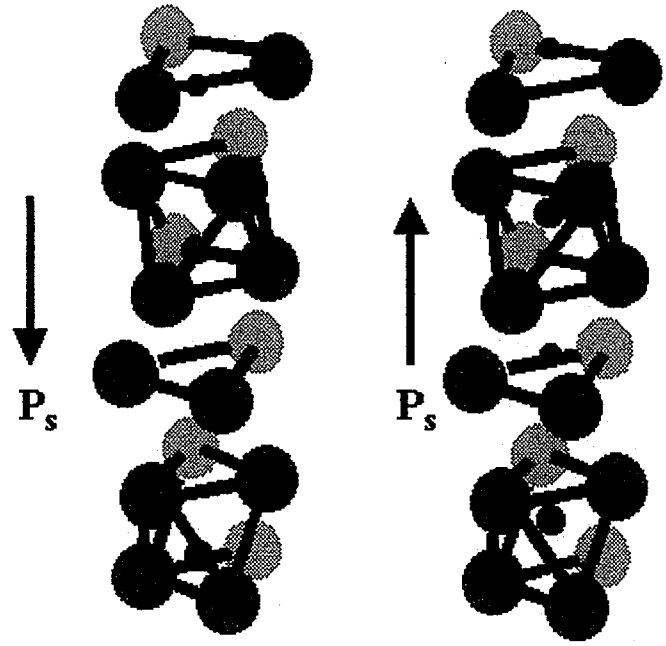

Figure 2.5. Illustration of $LiNbO_3$ crystal structure showing up and down domains; nibliums (red dot), lithiums (blue dot) and oxygen (aqua dot)

Chaper 3 Objectives

The purpose of our first project is to determine the electronic structure of tellurite glasses, which is the basis of their superior optical properties. Our study has focused on the structural development of glasses within the Li_2O- WO_3 - TeO_2 ternary system, which has shown promising optical properties. To accomplish the electronic structure of alkali tellurite glass system, we have used X-ray photoelectron spectroscopy.

The second project is to prepare transparent ferroelectric glass-ceramics, which have potentially large nonlinear optical properties at a much lower cost. Glass-ceramic nano-composites are investigated with varying $LiNbO_3$ content within the $(1+x)/2\ Li_2O + (1-x)/2\ Nb_2O_5 + 2x\ SiO_2$ (x= 0.4-0.9) series, which is equivalent to $x(Li_2O*2SiO_2) + (1-x)\ LiNbO_3$ pseudo binary glass system. Their crystallization, optical properties, and the effects of electric fields are studied.

Chapter 4 Experimental Methods

4.1 Compositions

4.1.1 Tellurite glasses

The glasses in this study were prepared (by Naval Research Laboratory) according to formula (a) $10Li_2O*xWO_3*(90-x)\ TeO_2$ and (b) $xK_2O*\ (10-x)\ Li_2O*25WO_3 * 65TeO_2$ (see Table 4.1). All glasses in this work also contained 0.1 wt % Tm_2O_3. In addition, tungsten free $20Li_2O*80TeO_2$ sample was used as a binary reference for XPS spectrum. The first glass series, $10Li_2O*xWO_3*(90-x)\ TeO_2$, emphasizes the substitution of tellurium by tungsten oxide with constant alkali oxide content. The glasses were prepared from reagent grade Li_2CO_3 (Alfa Aesar, Puratronic Grade, 99.999%), K_2CO_3 (Alfa Aesar, Puratronic Grade, 99.999%), WO_3 (Alfa Aesar, Puratronic Grade, 99.998%), TeO_2 (Alfa Aesar Puratronic Grade, 99.9995%) and Tm_2O_3 (Rhone-Poulenc, 99.90%). After mixing the appropriate compounds in 15 gram batch size, the powders were placed into a Thermolyne Type 1400 electric furnace. The mixture was first decomposed and then homogenized by heating to 850 °C in gold crucibles in air for 4 hours. After removing the sample from the furnace, the samples were allowed to cool at room temperature. The glasses were then annealed at 350 °C for 2 hours. To make the 20 $Li_2O*80\ TeO_2$ glass sample, the mixture was melted at 850 °C for 4 hours. After removing from furnace, the melt was quickly quenched in water. The reason for the quick quench was that this composition was just outside the glass-forming region.

4.1.2 Lithium niobate disilicate nano-composite glass-ceramics

The nominal compositions selected for making glass-ceramic nano-composites were $(1+x)/2\ Li_2O + (1-x)/2\ Nb_2O_5 + 2x\ SiO_2$ (x= 0.4-0.9), which are equivalent to $x(Li_2O*2SiO_2) + (1-x)\ LiNbO_3$ pseudo binary (see Figure 4.1). So the glasses were prepared according to formula $x(Li_2O*2SiO_2) + (1-x)LiNbO_3$, where lithium disilicate is gradually replaced by lithium niobate. The glasses were prepared from reagent grade Li_2CO_3 (99.9 %), SiO_2 (99.9 %) and Nb_2O_5 (99.99 %). After mixing the appropriate amounts, the mixture was first decomposed at 1100 °C and then melted by heating to 1500 °C in a platinum crucible for 2 hours in the electric furnace (Lindberg). Glass samples were cast by pouring the liquid into a 10 mm x 10 mm x 15 mm copper mold (preheated to ~ 300 °C). All the melt-quenched samples were light yellow, transparent glasses. The cast pieces were immediately transferred to annealing furnace preheated to 450 to 515 °C and annealed for 4 hours, depending on the composition. Then the furnace was turned off for cooling down to room temperature. The annealed samples were viewed with polarized light to check that they were stress-free. The samples were cut to 1.5 mm thickness for further experiments.

After cutting, the samples were attached to a sample holder for polishing. To polish optically flat, SBT (South Bay Technology) polishing tool was used, giving flat and transparent samples. Here, silicon carbide polishing pads (400, 600 grit, and 8 micron ultralap) were used for grinding and cerium oxide (CeO_2) was used with felt pad for polishing.

After polishing, the samples were subjected to crystallization thermal treatment. Based on thermal analysis data (Figure 4.2), the samples were heat treated at their glass transition (Tg) temperature for 12 to 24 hours. The samples were placed in the center of the furnace and heated at 13 °C per minute. After reaching the target heat treatment, the samples were cooled down to room temperature at 15 °C per minute.

To reinforce optical nonlinearity of these samples, the electric poling experiment was done. For this experiment, both sides of glass specimens were polished so that the sample was a plate of ~ 1.5 mm thickness. During thermal poling, the specimens were connected to electrodes made of platinum and were heated to Tg in the electric furnace under an applied dc voltage of 5 kV for 12 to 24 hours. The samples were then cooled down to room temperature inside the furnace and then the dc voltage was removed.

4.2. Characterization

4.2.1 Structure of tellurite glasses

The structure of the *in situ* fractured glass samples was determined by X-ray photoelectron spectroscopy (XPS), which is a very powerful technique to study the chemical and electronic bonding states of a sample.

For this experiment, a high resolution ESCA Scienta 300 spectrometer was used (Figure 4.3) in which photoelectrons are excited by monochromatic Al-Kα X-rays of energy, 1486.6 eV as the probe radiation. The photoelectrons emitted from freshly *in situ* fractured surface are collected by an electrostatic lens system and their kinetic energy

(E_k) is measured with a hemispherical analyzer. The binding energy (E_B) is then obtained from

$$E_k = h\upsilon - E_B - \varphi$$

where $h\upsilon$ is the energy of the x-rays (Figure 4.4) and φ is the work function of the spectrometer. The work function depends on the surface barrier of the analyzer/detector, and can be estimated through proper calibration. Thus, each element gives rise to a characteristic set of peaks in the photoelectron spectrum at kinetic energies determined by the photon energy and the respective binding energies.

The XPS samples were ground to 1 mm thickness to give a flat surface for proper clamping of sample holder in the chamber. They were then fractured *in situ* in the ultra high vacuum (UHV) preparation chamber where the base pressure was on the order of 10^{-9} Torr. This procedure avoided any contamination layer from reaction with the ambient on the fractured glass surface. After fracturing of the samples, XPS data were obtained immediately from the newly created surface. The photoelectrons were generated from the fracture surface which has area of about 3 x 1 mm^2. The X-ray spot size was about 1.6 x 0.3 mm^2.

The ESCA instrument was operated for survey scans over the entire binding energy range as well as for the regional scans over the photoelectron peaks of interest. Our regions of interest were tungsten 4f (45~30eV), oxygen 1s (540~525eV), tellurium 3d (585~565eV), carbon 1s (300~275eV), lithium 1s (65~50eV), and valence band (25~0eV). An energy step size of 0.1eV was used for the regional scans and the energy resolution was determined at the Fermi edge of Ag metal. At this level of resolution, the

instrumental contribution to the line width was extremely small (< 4%). Then the experimental widths were primarily a combination of charging and natural line widths. Number of scans was adjusted to give high signal to noise ratio. For our samples, average number of scans was about 6 to 8 times.

Since glass samples are insulator, the glass surface exposed to the x-rays becomes positively charged due to the emission of photoelectrons. In order to compensate for this charging effect, the sample surface was flooded with low energy electrons of about 4 – 8 eV. For this purpose, an electron flood gun supplied the electrons at an incidence angle of 45°. Under these optimum conditions, the fracture surface was at a slightly negative potential with respect to the ground. It gives a better resolution and reproducibility than the surface of neutral potential.

After scanning each region, XPS data were collected by the microcomputer and then analyzed using the software provided by the spectrometer manufacturer. The binding energy of the spectral peaks, relative element peak position, and their corresponding peak areas were determined using the Scienta software. A Shirley background was subtracted and a Voigt line shape, which is a mixture of Gaussian and Lorenzian was used to analyze the peaks for each specific element of spectra. Measured binding energy of the peaks was corrected based on the calibration factor calculated from the difference between the measured binding energy of the C 1s peak and its reference value of 284.6 eV.

4.2.2 Nano-composite glass-ceramics

The annealed glass samples were investigated with differential thermal analysis to determine their glass transition temperature (Tg) and crystallization temperature (Tx) (Table 4.2). Tg is the temperature at which the sample transforms from solid to liquid state and Tx is the temperature at which glass crystallization rate is maximized. A stable glass should have the difference (Tx –Tg), which is higher than 10 °C.

A small amount (~ 500 mg) of glass pieces was weighed and placed in a small Al_2O_3 crucible inside the TG/DTA analyzer (Model STA 409C, Netzsch Instruments, Paoli, PA). Each sample was subjected to a heating rate of 10 °C/min up to a temperature of 1100 °C in air atmosphere. The sample was cooled at a rate of 15 °C /min to room temperature. The change of heat flow as a function of temperature was measured.

Tg was determined by the intersection of the tangent of baseline with the tangent line to the inclined of heat absorption curve ((a) in Figure 4.2). Tx was also determined by the intersection of the tangent line of the baseline with the tangent line to the exothermic peak ((b) in Figure 4.2). The error for the thermal properties is $\pm$ 1.5 °C. Based on the glass transition temperature (Tg) and crystallization temperature (Tx), these samples were heat treated in the electric furnace for different durations. More details for the samples' thermal analysis and their heat treatment are given in the Results section.

The progress of crystallization in heat-treated samples was determined by X-ray diffraction (XRD) analysis using Cu Kα radiation on a diffractometer (Rigaku). The XRD patterns were analyzed to identify the crystalline phases and any texture on the glass surface. They were indexed and matched of possible phases using JCPDS (Joint

Committee on Powder Diffraction Standards) database on computer. XRD patterns of all samples were recorded at a scanning rate of 1.5 degree/min over a 2θ range of 15 – 75° with the diffractometer operated at 50 kV and 100 mA.

To obtain higher resolution microstructure of the surface of heat-treated glasses, a JEOL 6300F scanning electron microscope (SEM) was used with a field emission gun. The uncoated specimens were examined under a 5 kV accelerating voltage.

The energy dispersive spectrometer (EDS) detector in the SEM was employed for the identification of nano-crystalline phase in the glass-ceramics. In the SEM sample chamber, the EDS captures X- rays that are emitted when highly focused electron beam impinges on the sample surface. The characteristic X-rays are used to determine the elemental composition of the surface features. The X-ray analyzer was used in the point, line and area (X-ray map) scan modes. Since crystalline phases were small, qualitative X-ray maps were found to be more useful than the quantitative analysis. JEOL 6300 F was also used to obtain secondary electron images of the glass surface.

Transmission electron microscopy (TEM) specimens were prepared using a powder method. In brief, a section of sample, either the bulk or surface, was selected then crushed in an alumina mortar. The resulting powder was put in suspension in acetone using an ultrasonic vibrator. A drop of the suspension was set on a 200 mesh 3 mm diameter copper grid. The specimens were studied using a JEOL 2010 FEG TEM operated at 200 kV. Imaging mode was employed in conjunction with the diffraction mode.

Second harmonic generation studies were carried out by a pulsed Nd:YAG laser. The SHG optical properties were determined with transparent, well polished, and heat-treated sample. The incident laser with wavelength of radiation (ω), 900nm was used with a pulse width of 65 fs. The experimental setup is shown in Figure 4.5. Two different incident powers, I_ω = 740 and 826 mW, were used in this experiment.

Table 4.1. Glass composition and glass transition temperature.

Composition (mol %)	Glass Transition Temperature (Tg)
$20Li_2O*80TeO_2$	259 °C
$xK_2O*(10-x)Li_2O*25WO_3*65TeO_2$	
x = 0	335 °C
5	331 °C
10	339 °C
$10Li_2O*xWO_3*(90-x)TeO_2$	
x = 5	283 °C
10	304 °C
15	321 °C
20	334 °C
25	335 °C

Table 4.2. Glass composition and Their differential thermal analysis.

x	composition(mol%)			T_g(C)	T_x(C)
	Li_2O	Nb_2O_5	$2SiO_2$		
0.3	40.6	21.9	37.5	563.3	731.3
0.4	38.9	16.7	44.4	561.5	739.7
0.5	37.5	12.5	50	553	742
0.6	36.4	9.1	54.5	544.5	744
0.7	35.4	6.3	58.3	528.2	748

* The error for the thermal properties is $\pm$ 1.5 °C

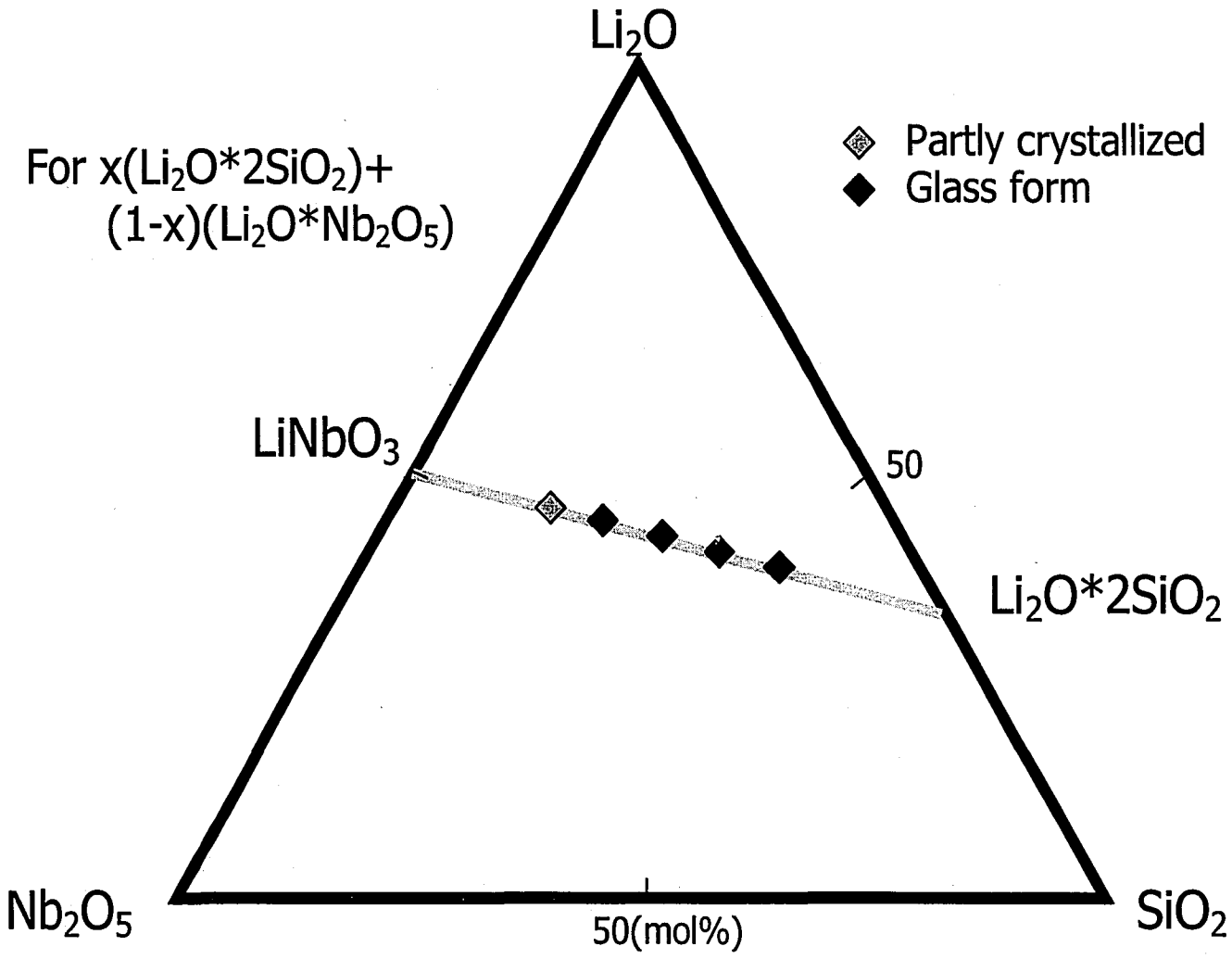

Figure 4.1. The nominal compositions for glass-ceramic nano-components are (1+x)/2 Li_2CO_3 + (1-x)/2 Nb_2O_5 + 2x SiO_2 (x= 0.3 - 0.9).

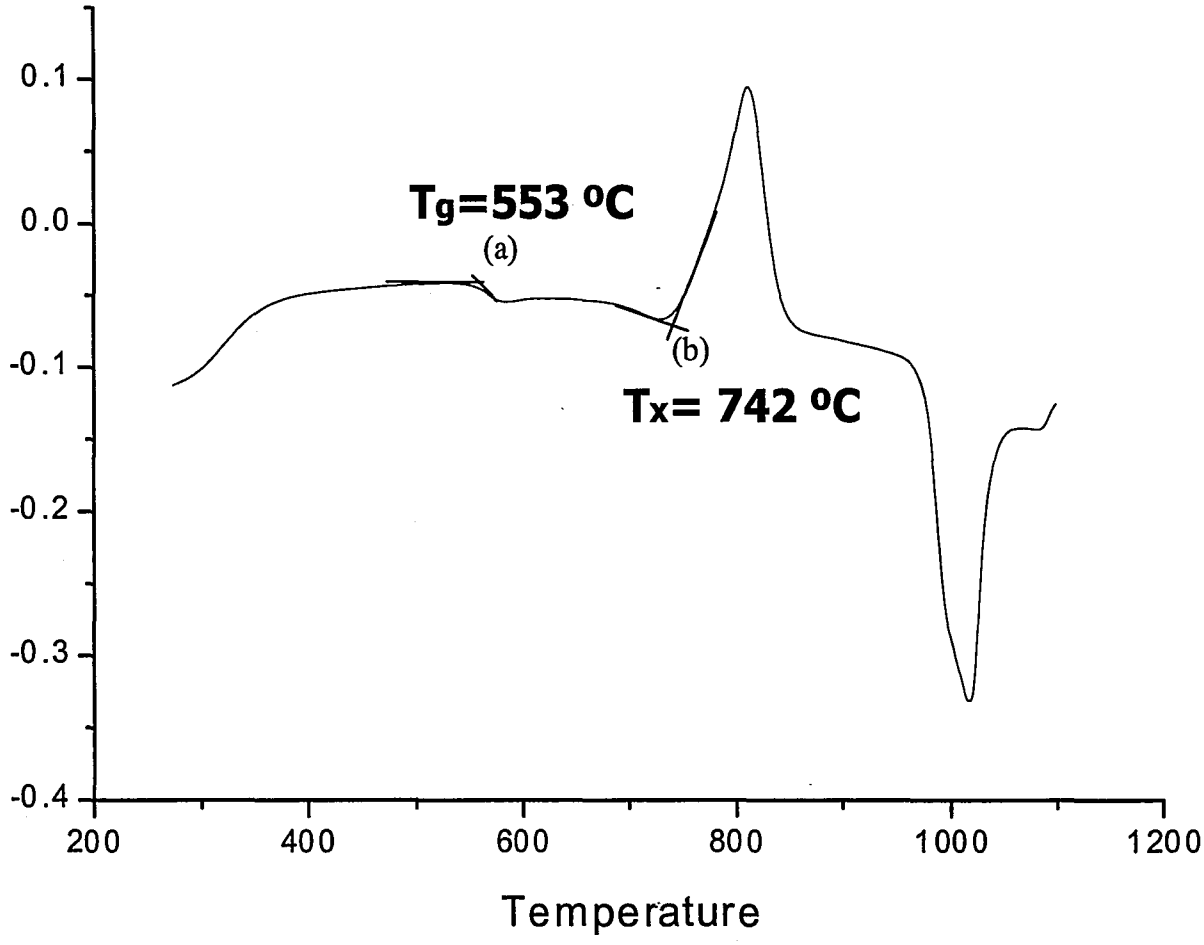

Figure 4.2. Thermal analysis data showing Tg and Tx for (1+x)/2 Li_2O * (1-x)/2 Nb_2O_5 * 2x SiO_2 glass with x= 0.5.

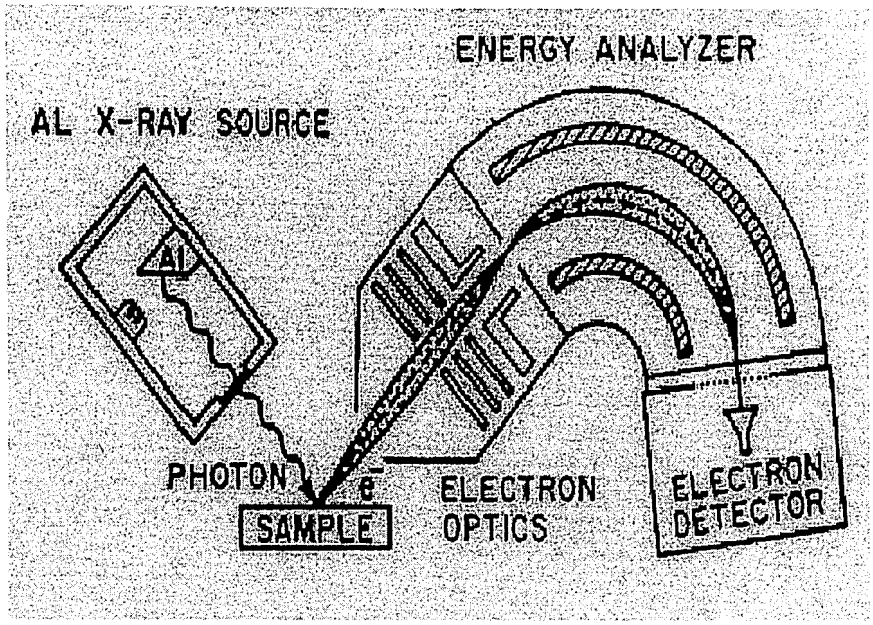

(a)

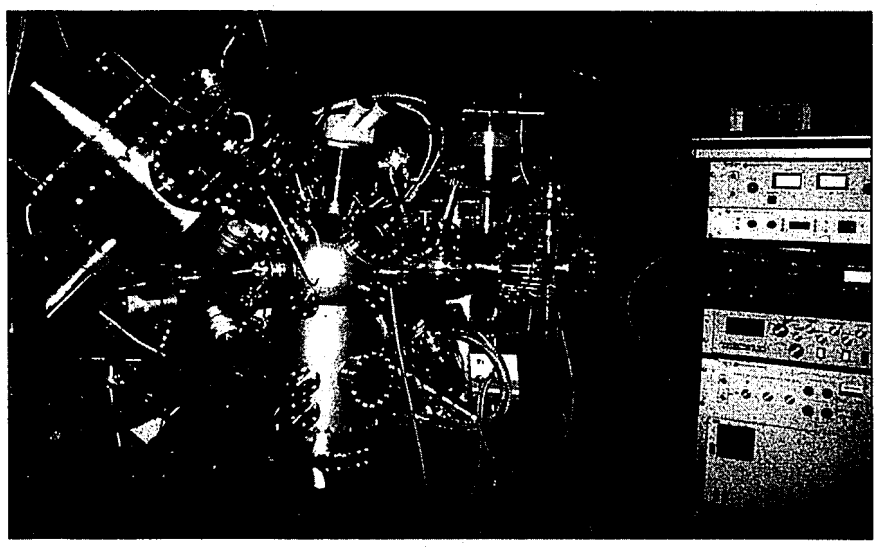

(b)

Figure 4.3. (a) Schematic representation of the typical experimental arrangement in ultra high vacuum for XPS. (b) A high resolution ESCA Scienta 300 spectrometer used for this experiment.

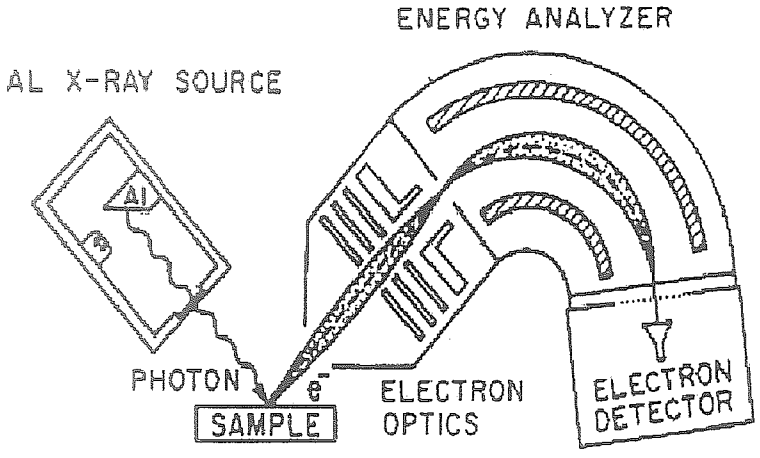

(a)

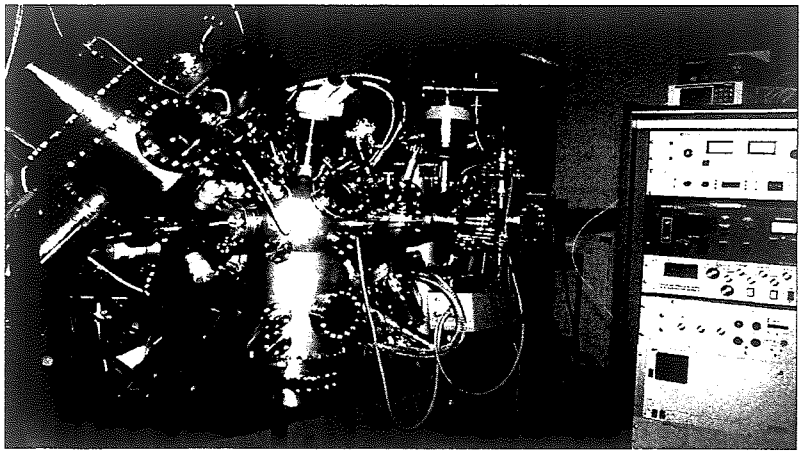

(b)

Figure 4.3. (a) Schematic representation of the typical experimental arrangement in ultra high vacuum for XPS. (b) A high resolution ESCA Scienta 300 spectrometer used for this experiment.

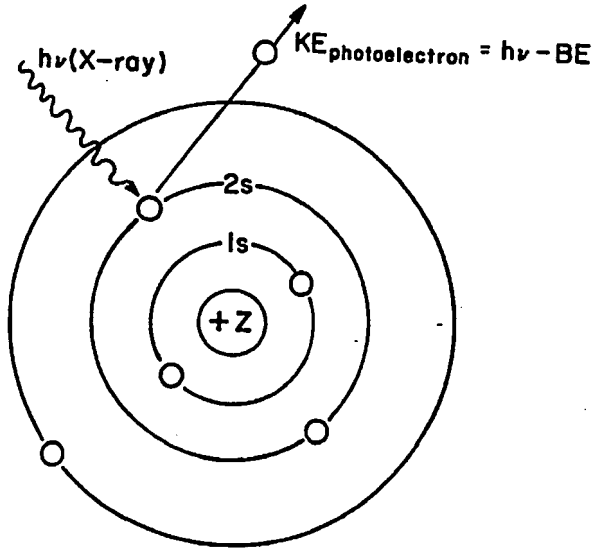

Figure 4.4. The photon (X-ray) is absorbed by an atom in a molecule or solid, leading to ionization and the emission of a core electron. Incident photon transfers its entire energy to a bound electron.

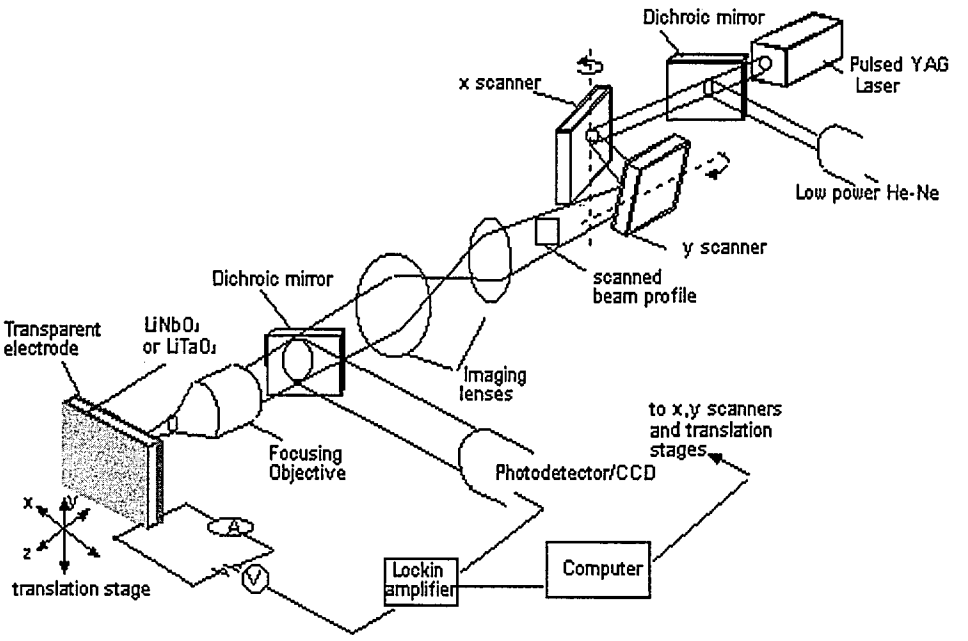

Figure 4.5. SHG experimental setup by using a pulsed Nd:YAG laser.

Chapter 5 Results

5.1 Tellurite glasses

The differential thermal analysis of (a) $10Li_2O*xWO_3*(90-x)\ TeO_2$ and (b) $xK_2O*(10-x)\ Li_2O*25WO_3*65TeO_2$ glasses was conducted to determine the glass transition temperature (Tg) (Table 4.1). The results for the $10Li_2O*xWO_3*(90-x)\ TeO_2$ glass series show that Tg increases monotonically with increasing WO_3 concentration (Figure 5.1). It increases from 283 °C for a glass containing 5 mol % WO_3 up to 335 °C when the concentration of WO_3 is increased to 25 mol %.

Figure 5.2 shows the O 1s X-ray photoelectron spectra for the$10Li_2O*xWO_3*(90-x)TeO_2$ glass system. Note that each peak is symmetrical and there is no shoulder on the larger binding energy side of the main peak. However, as shown in Figure 5.3, the main O 1s peak shifts toward higher binding energy with increasing WO_3 content except perhaps for the glass with 15 % WO_3, which shows a smaller increase. The shape of the main peak is similar for all compositions as shown in Figure 5.4. Heo et al.[5] reported observing a shoulder on the higher binding energy side of the O 1s photoelectron spectrum of alkali tellurite glasses. They attributed this shoulder (~ 538 eV) to the oxygen atom in TeO_3 trigonal pyramids (tp) and the main peak at ~ 536 eV to that in TeO_4 trigonal bipyramids (tbp). Himei *et al.* [25] also observed a shoulder on the high binding energy side of the main O1s peak in the photoelectron spectra for the $xLi_2O*(100-x)\ TeO_2$ glass surfaces that were exposed to air. However, they did not find the

shoulder, as in the present case, when the sample was fractured in the vacuum, thus confirming the high quality of our data.

Figure 5.5 shows Te 3d photoelectron spectra for the samples in the same system. Two peaks are observed in the Te 3d spectra, the higher binding energy peak is due to Te $3d_{3/2}$ and the lower binding energy peak is due to Te $3d_{5/2}$. Both peaks shift to higher binding energy with increasing WO_3 as shown in Figure 5.6 for Te $3d_{5/2}$.

The W 4f X-ray photoelectron spectra for the samples are shown in Figure 5.7. The shape of the peaks is nearly the same for all values of x, but the position shifts as for the other core level spectra. The observed binding energy and full width at half maximum (FWHM) for the core level O 1s, Te $3d_{5/2}$ and W $4f_{7/2}$ peaks for our glass samples are listed in Table 5.1. Experimental uncertainty in the binding energies is less than ± 0.1eV. Finally, Figure 5.8 shows the valence band spectra for the glasses in the $10Li_2O*xWO_3*(90-x)\ TeO_2$ system. The bottom curve is for α-TeO_2 crystal taken from Himei *et al.*[25].

The O 1s and W 4f photoelectron spectra for the mixed alkali $xK_2O*(10-x)\ Li_2O*25WO_3*65TeO_2$ glass system are shown in Figure 5.9 (a) and (b), respectively. The observed binding energy and FWHM are given in Table 5.1. Since the C 1s spectrum of the 5% and 10 % K_2O containing glasses showed an additional C 1s peak other than the reference C 1s peak (284.6 eV) due to contamination (Figure 5.10), the Te $3d_{5/2}$ peak (~ 576.05 eV) has been used as an internal reference. The O 1s and W 4f peaks shift toward smaller binding energy when lithium is replaced by potassium (Figure 5.9). Each peak is symmetrical and there is no shoulder on the low or high binding

energy side of the main peak. The shape of the peak is nearly the same for all values of x.

5.2 Ferroelectric Glass-ceramics

Within the $x(Li_2O*2SiO_2)$ * (1-x) $LiNbO_3$ glass system, we established an extensive glass forming region as shown in Figure 4.1. Initially, glass formation was determined through visual inspection. Clear glasses were obtained with as little as x = 0.4. Glasses with higher lithium niobate content exhibited partial crystallization. Compositions described as partially crystallized formed both a clear glass and an opaque crystalline layer at the top and bottom faces of the sample. Faster plate-quenched method is needed to make glass of such compositions e.g. the one containing 70 % lithium niobate. Clear glasses were formed with x = 0.6 without the need of rapid quenching as shown in Figure 4.1.

Samples for x = 0.3 to 0.9 were prepared and then analyzed by DTA to find the glass transition temperature (Tg) and crystallization temperature (Tx). Figure 5.11 shows DTA data of samples for each x value. Exothermic direction is pointing upward in the figure. The glass transition and crystallization temperature are then found by using tangent lines for each peak, as explained in Figure 4.2. The values of Tg and Tx for each sample are listed in Table 4.2 and displayed in Figure 5.12 as a function of x value. The data indicate that the glass transition temperature decreases when disilicate fraction increases, but crystallization temperature increases. It means that the higher the value of

x (the glass has more silica), the glass is more difficult to crystallize. In other words, glass forming ability decreases with increasing lithium niobate.

X-ray diffraction technique was used to identify the crystalline phase and its texture on the heat treated surface. Figure 5.13 shows X-ray diffraction data for sample that had 50 % of lithium niobate and 50% of lithium disilicate (x = 0.5). This sample was heat treated at 695 °C for 1 hour, 6 hours, 12 hours, and 24 hours. Our reference for the diffraction peaks of lithium niobate crystalline powder is taken from the JCPDS file 20-0631[43] (Figure 5.13). For lithium disilicate our data are compared with JCPDS file 24-0651[44]. The 1 hour heat treated sample did not show any peak indicating that there was no crystallite present in the glass. As heat treatment time became longer, several peaks appeared. These peaks show that there were different kinds of crystallites present in the devitrifying sample. Some peaks are due to lithium niobate whereas others arise from lithium disilicate. An unknown (X) crystalline phase was also found in the sample. Only the sample heat treated for 1 hour was transparent, the samples heat treated for longer time appeared translucent due to the presence of crystallites.

Figure 5.14 shows X-ray diffraction data for the glass containing 60 % of lithium niobate and 40% of lithium disilicate (x =0.4) heat treated at 650 °C for 3 hours. After heat treatment, the sample was translucent with a light yellow color. XRD of this sample shows the presence of lithium niobate and other crystallites. To determine whether or not devitrification occurred primarily on the surface, the sample was ground ~ 275 μm and then again its XRD pattern was studied. Note that the intensity of peak has decreased and

some peaks have disappeared. After grinding 400 μm, there are no diffraction peak observed from the sample.

Figure 5.15 shows XRD pattern of two samples that were composed of 60 % lithium niobate and 40% lithium disilicate, and heated at 560 °C for 12 hours with thermal poling. The specimens were in physical contact with the platinum electrodes. One sample was heat treated without thermal poling and the other one was heat treated under the electric field, $E = 1.5*10^5$ V/m during the heat treatment. They were both transparent after thermal poling, and there was no visible difference between them. Figure 5.15 shows the XRD pattern for (a) the heat treated sample without electric field and (b) for the heat treated sample with poling. They both show high intensity of lithium niobate peak at $2\theta = \sim 38.99$ degree, and lower intensity peaks of another phase, most likely lithium disilicate.

Heat-treated glass samples with $x = 0.4$ have been examined for microstructural analysis. For the sample with $x = 0.5$ that was heat treated at 695 °C for 1 hour, 6 hours, and 24 hours, the microstructure was studied by scanning electron microscope (SEM) after etching the samples with 1% HF for 20 seconds, as shown in Figure 5.16. The figure shows the development of crystalline phase with heat-treated time. In Figure 5.16 (a) for the sample heat treated for 1 hour, we only see homogeneous clear polished glass surface. However, 6 h and 24 h heat-treated samples in figure (b) and (c) show sub micron, nano sized crystallites. The longer is the heat-treated time, the larger and more numerous are the crystallites.

Thermally poled samples were also analyzed by scanning electron microscope. Figure 5.17 shows microstructures of such a sample, indicating the effect of poling on the microstructure. Figure 5.17(a) and (b) show the microstructure of unpoled glass-ceramics and less than 0.5 μm size crystallites were observed on the bulk samples. On the other hand, Figure 5.17 (c) and (d) show the different orientation of crystallites on the sample that was heat treated with electric field. Even though crystallites have similar size in Figure 5.17 (a) and (c), the crystallites of the later are elongated and appear connected with each other like branches.

The TEM experiments were conducted on a sample composed of 60 % lithium niobate and 40 % lithium disilicate and heated at 560 °C for 12 hours under electric field. The X-ray diffraction (XRD) experiments revealed that this sample contains crystalline lithium niobate and lithium disilicate phases. However, XRD is a statistical characterization method; the TEM experiments were conducted in order to determine where the crystallization takes place.

The high-resolution images (HRTEM) of the bulk exhibit only an amorphous (apparently phase separated) structure that is characteristic of this glass (Figure 5.18 (a)). Figure 5.18 (b) displays a typical image with its fast Fourier transform (FFT). The FFT is a mathematical tool that allows to reconstruct the diffraction pattern of an image from the real image. As expected in the case of non-crystalline material, the FFT only shows diffuse rings as shown in Figure 5.18 (b). Figure 5.18 is taken from the center of the heat-treated sample.

Figure 5.19 shows HRTEM images of the heat-treated sample surface. Although most of the material is amorphous and exhibits the same worm-like feature and diffuse rings in the reciprocal space as seen in the bulk, some areas show the presence of crystallites (Figure 5.19 (a)). The different fringes observed in this figure correspond to the different atomic layers that comprise the crystalline part of the sample. Figure 5.19 (b) displays the FFT of the Figure 5.19 (a). This figure exhibits several spots of high intensity non-symmetrically distributed in the Fourier-space (reciprocal space) which are typical of a polycrystalline sample. Additionally, the analysis of the crystallite size showed that these areas are formed with a nano-sized grain.

The SHG optical property was measured by a pulsed Nd:YAG laser. Seven samples were prepared for this experiment. The samples were composed of 60 % lithium niobate and 40% lithium disilicate, and heated at 560 °C for 12 hours. Sample number # 1 to # 4 were under the electric field and sample # 5 to #7 were without thermal poling. The spot size was 100 μm and the used spots were different. Table 5.2 shows the result of each sample. Table 5.2 (a) presents SHG results for 740 mW ($=I_{\omega}$) incident power and Table 5.2 (b) with 826 mW incident power. The table shows that various values of SHG have no clear correlation with the sample treatment. Here is a large scatter in the values of SHG measured on different spots on the same sample. For example, for sample # 2 the SHG signal ranged 2 – 200 mV at different spots. Therefore, it is difficult to conclude whether or not thermal poling enhances SHG.

Table 5.1. Binding energy of XPS O1s, Te $3d_{5/2}$ and W $4f_{7/2}$ peaks for glass samples. Experimental uncertainties of the binding energies are less than ± 0.1eV.

Composition (mol %)	Binding Energy (eV)		
	O1s	Te $3d_{5/2}$	W $4f_{7/2}$
$20Li_2O*80TeO_2$	529.8 (1.27)[a]	575.7 (1.13)[a]	-
$xK_2O*(10-x)Li_2O*25WO_3*65TeO_2$			
x = 0	530.7 (1.31)	576.6 (1.25)	35.8(0.98)
5	530.2 (1.31)	576.0 (1.26)	35.1 (0.94)
10	530.2 (1.28)	576.2 (1.18)	35.2 (0.92)
$10Li_2O*xWO_3*(90-x)TeO_2$			
x = 5	530.4 (1.34)	576.2(1.2)	35.2 (0.93)
10	530.5 (1.3)	576.4 (1.18)	35.5 (0.92)
15	530.5(1.27)	576.3 (1.13)	35.3 (0.87)
20	530.6 (1.32)	576.5 (1.26)	35.5 (1.02)
25	530.7 (1.31)	576.6 (1.25)	35.7 (0.98)

[a] Full width at half maximum is given in parentheses

Table 5.2. SHG measurement for 60 % lithium niobate and 40% lithium disilicate, and heated at 560 °C for 12 hours samples. # 1 to # 4 samples were under electric field and # 5 to # 7 were not.

(a) SHG Measurement with 740 mW ($=I_{\omega}$) incident power

Sample	SHG Signal (micro-volt) $\propto (I_{2\omega})$	$I_{2\omega} / (I_{\omega})^2$ ($X 10^{-6}$)
#1	0.0	0
#2	2.7	4.9
#3	19.5	35.6
#4	1.6	2.9
#5	196.7	359.2
#6	2.76	5.0
#7	0.0	0.0

(b) SHG Measurement with 826 mW($=I_{\omega}$) incident power

Sample	SHG Signal (micro-volt) $\propto (I_{2\omega})$	$I_{2\omega} / (I_{\omega})^2$ ($X 10^{-6}$)
#1	96.6	141.6
#2	54.5	79.9
#3	27.4	40.2
#4	66.90	98.1
#5	168.4	246.8
#6	13.94	20.4
#7	17.0	24.9

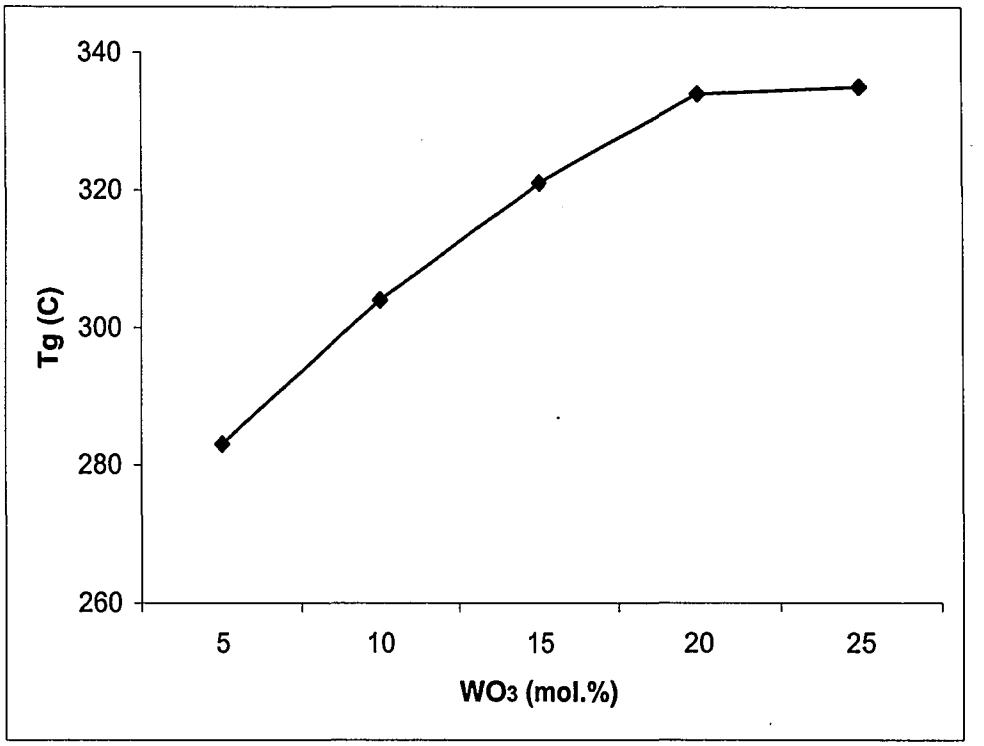

Figure 5.1. Glass transition temperature (Tg) of $10Li_2O*xWO_3*(90-x)TeO_2$ glasses.

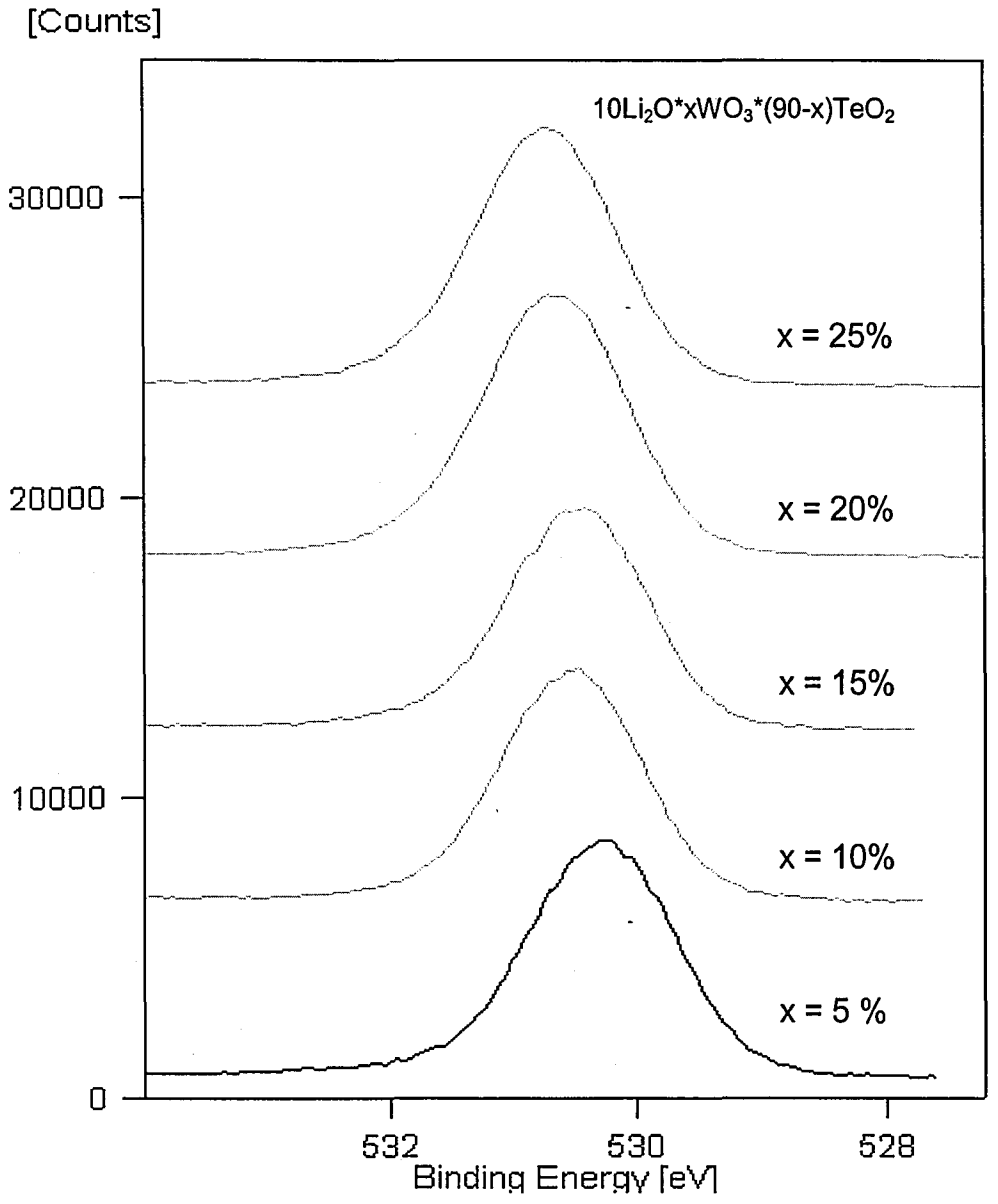

Figure 5.2. O 1s X-ray photoelectron spectra for the $10Li_2O*xWO_3*(90-x)TeO_2$ glass system.

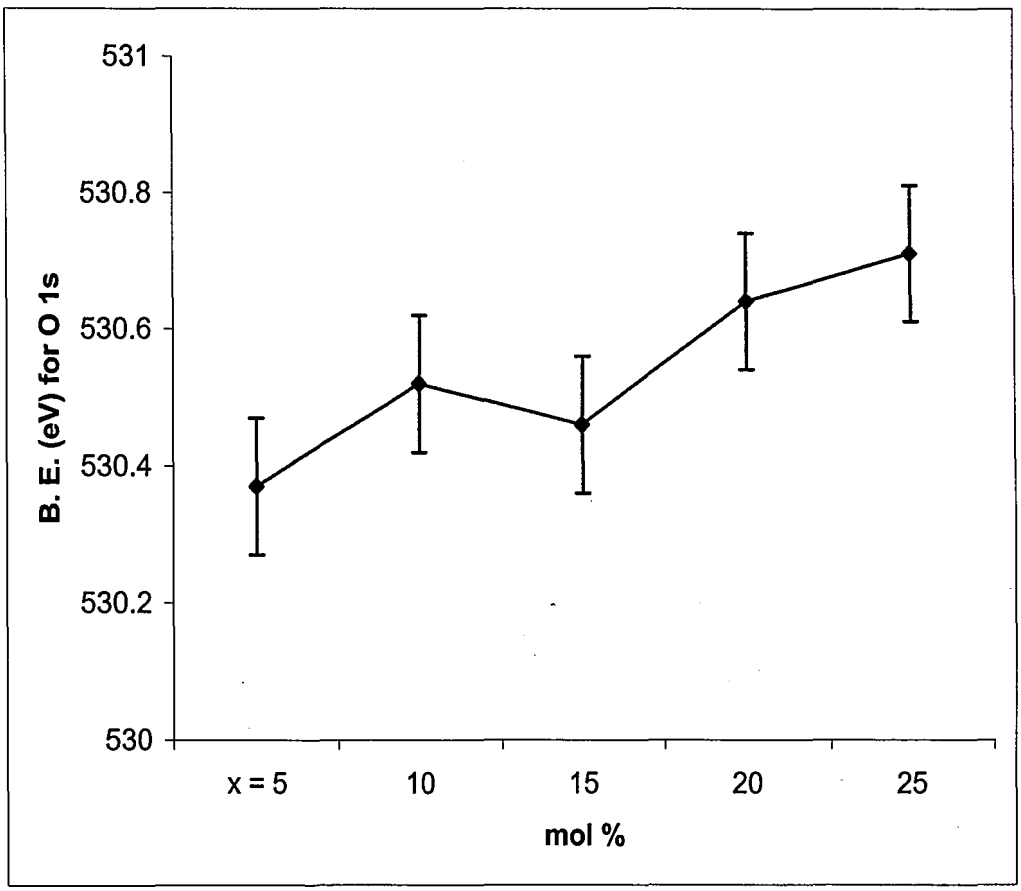

Figure 5.3. . The main O 1s core level peak position for the $10Li_2O^*$ xWO_3 $^*(90\text{-}x)$ TeO_2 glass system.

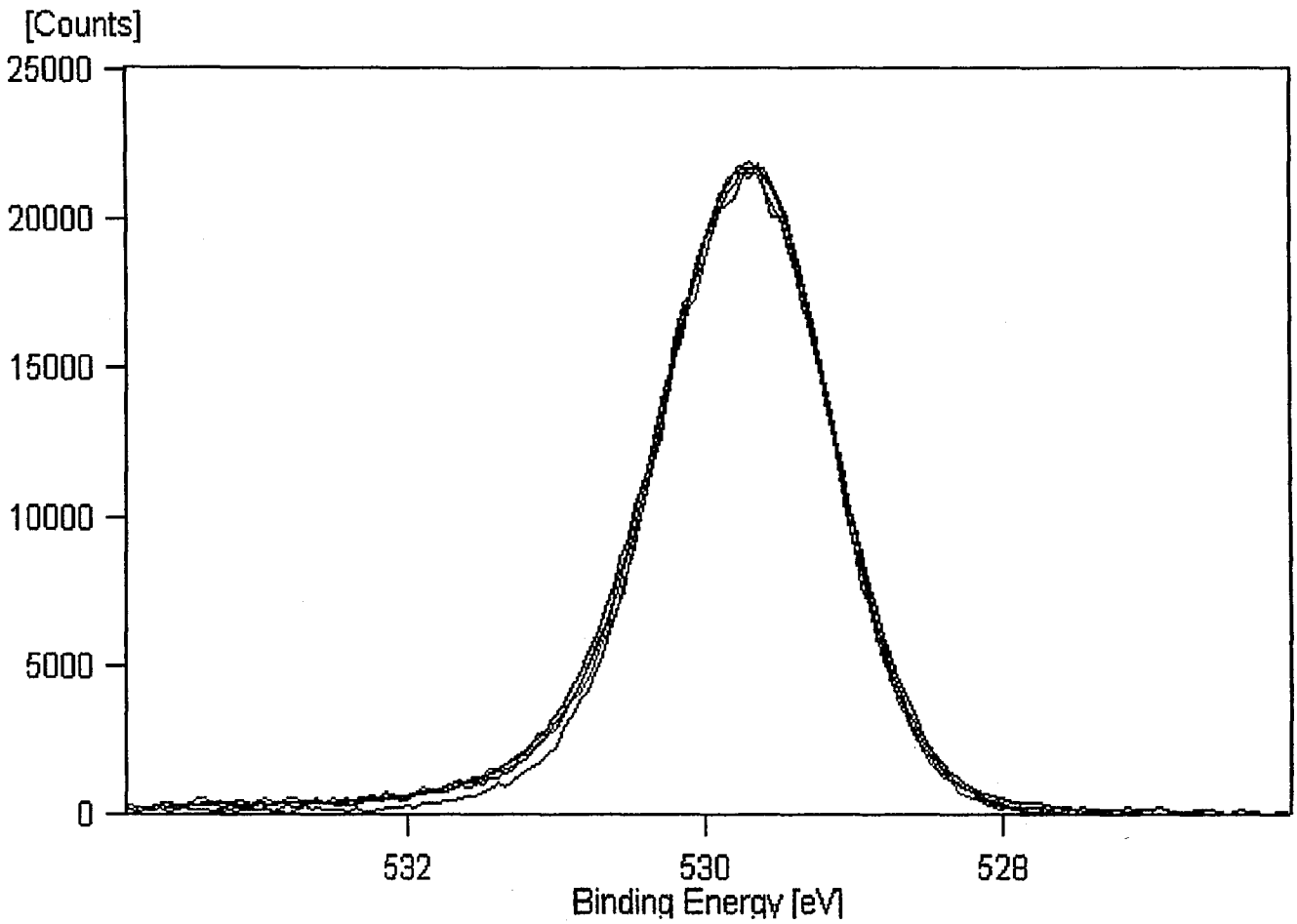

Figure 5.4. The shape of the O 1s main peak is compared with all compositions.

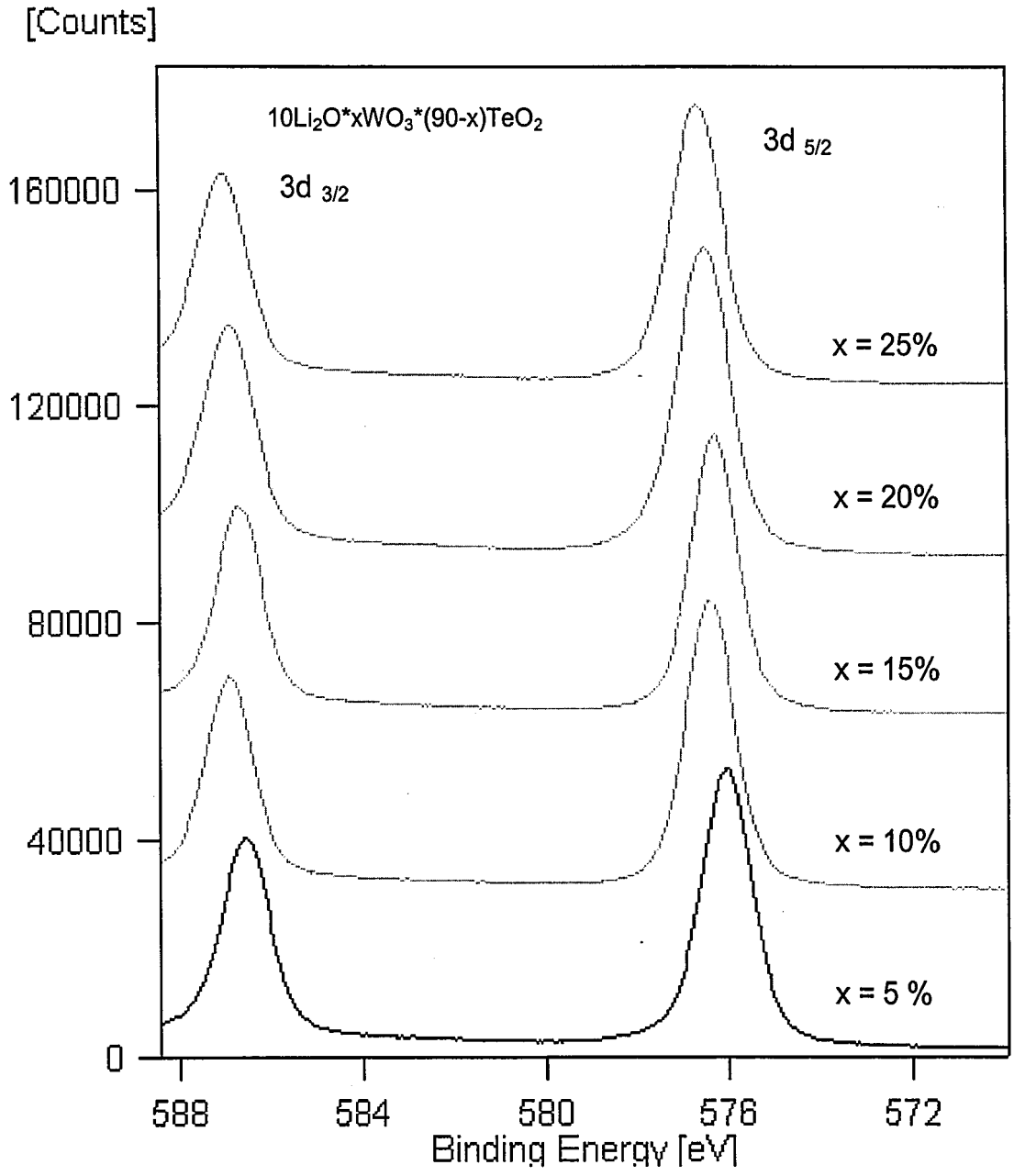

Figure 5.5. Te 3d X-ray photoelectron spectra for the $10Li_2O*xWO_3*(90-x)TeO_2$ glass system.

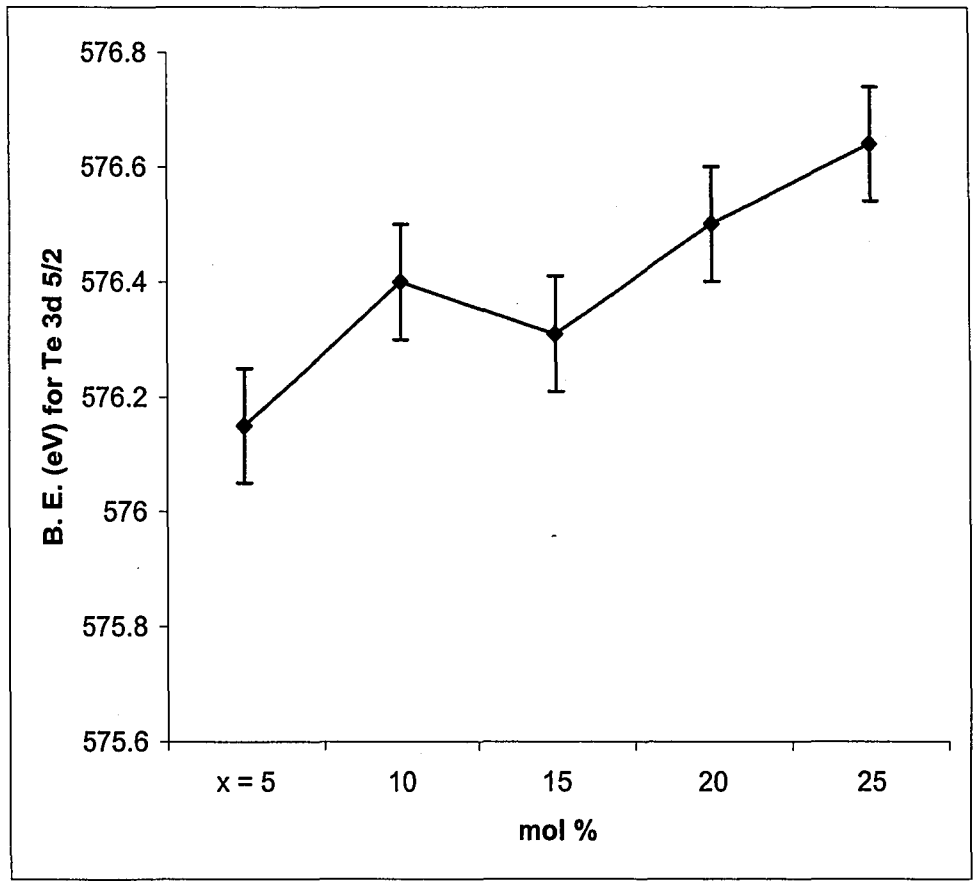

Figure 5.6. The main Te $3d_{5/2}$ core level peak position for the $10Li_2O^*$ xWO_3 $^*(90\text{-}x)$ TeO_2 glass system.

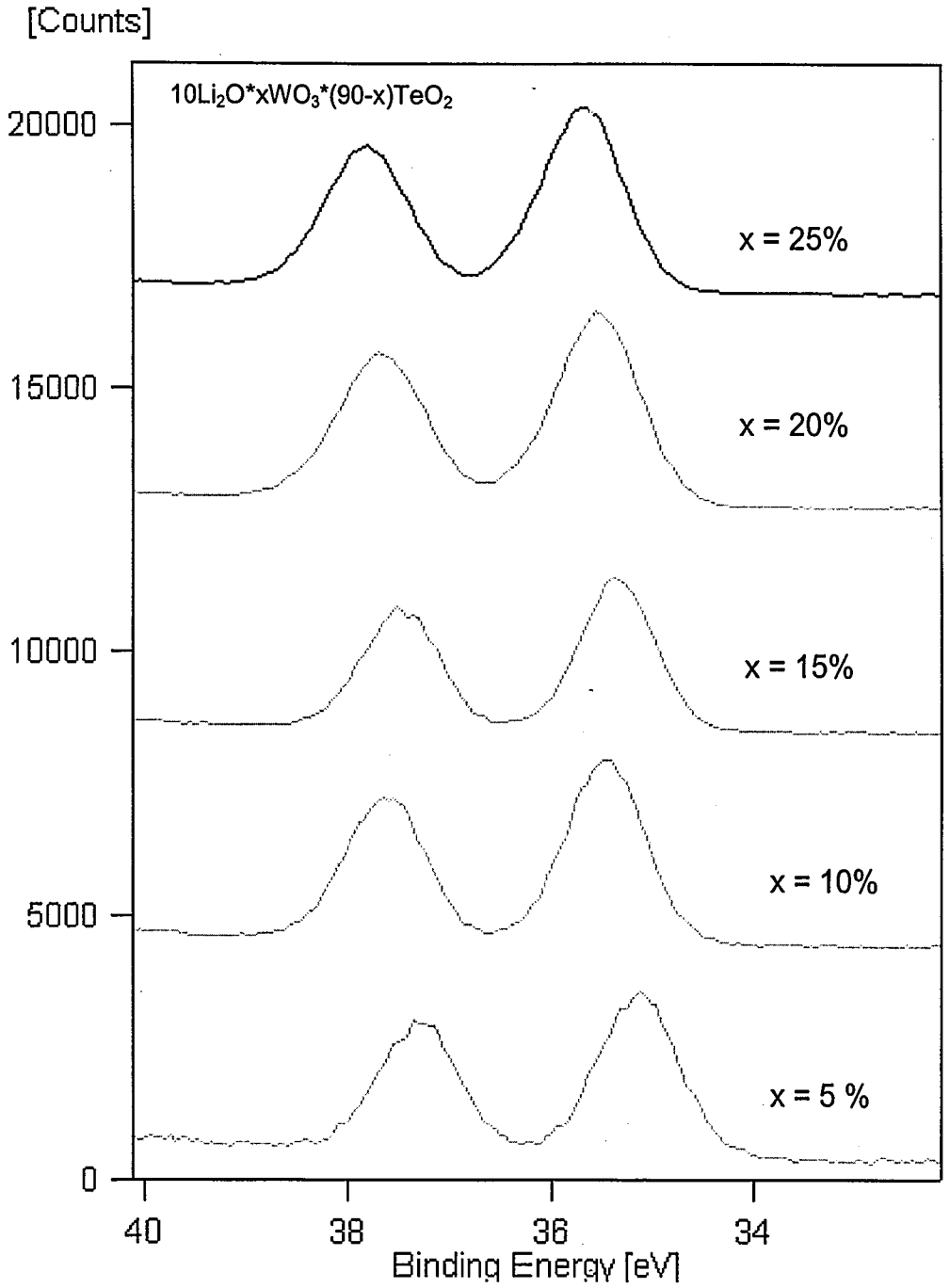

Figure 5.7. W 4f X-ray photoelectron spectra for the $10Li_2O*xWO_3*(90-x)TeO_2$ glass system.

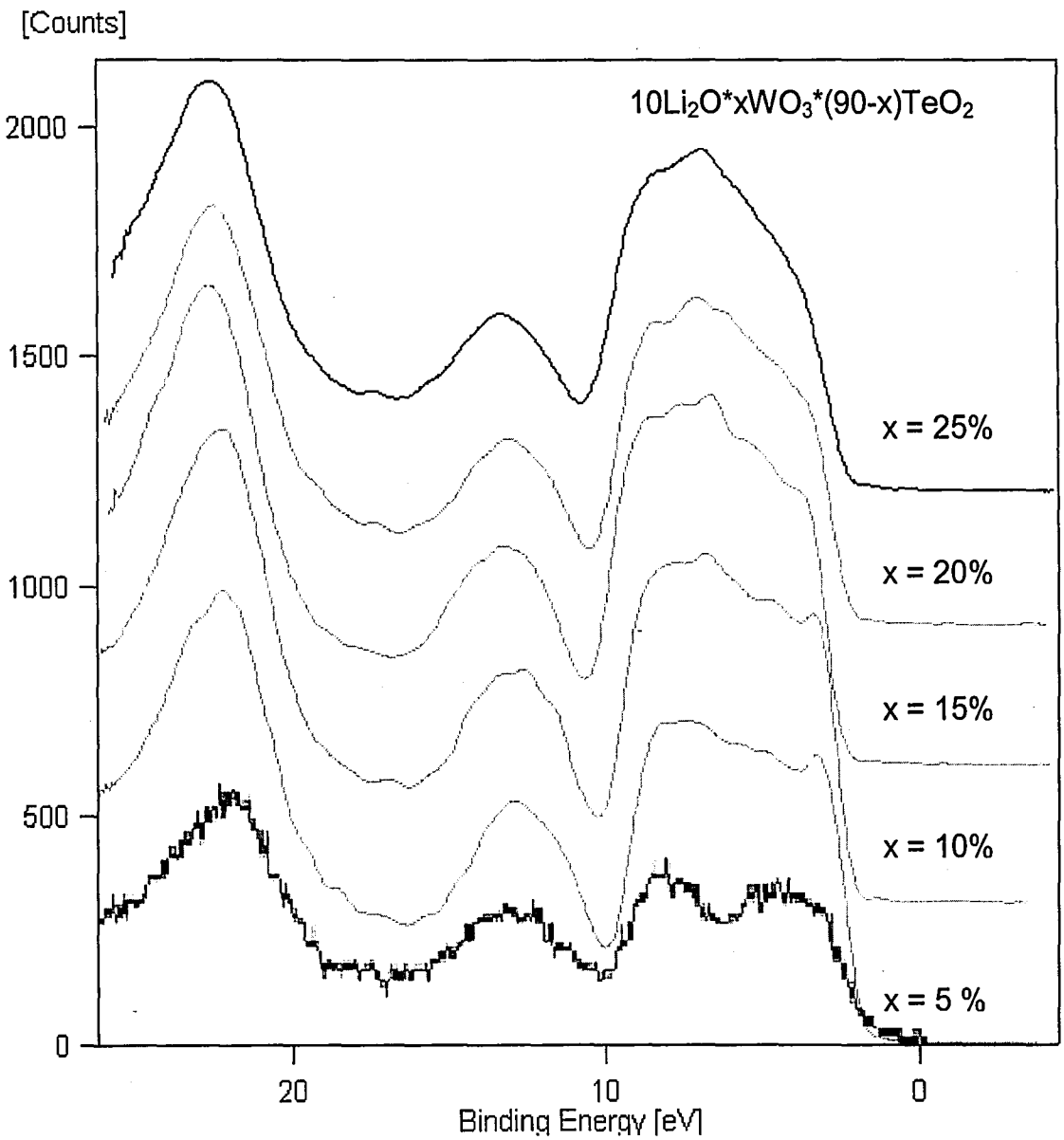

Figure 5.8. X-ray photoelectron spectra near the valence band of $10Li_2O*xWO_3*(90-x)TeO_2$ glass system. The bottom curve is for α-TeO_2 crystal taken from Himei *et al.*[25].

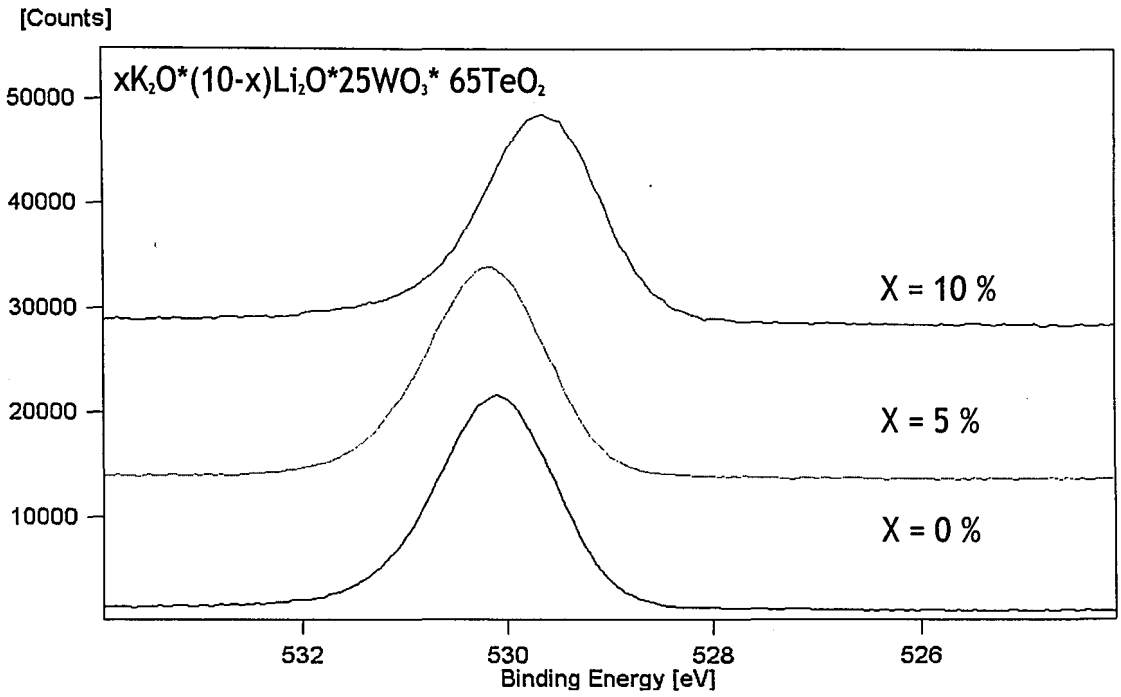

(a)

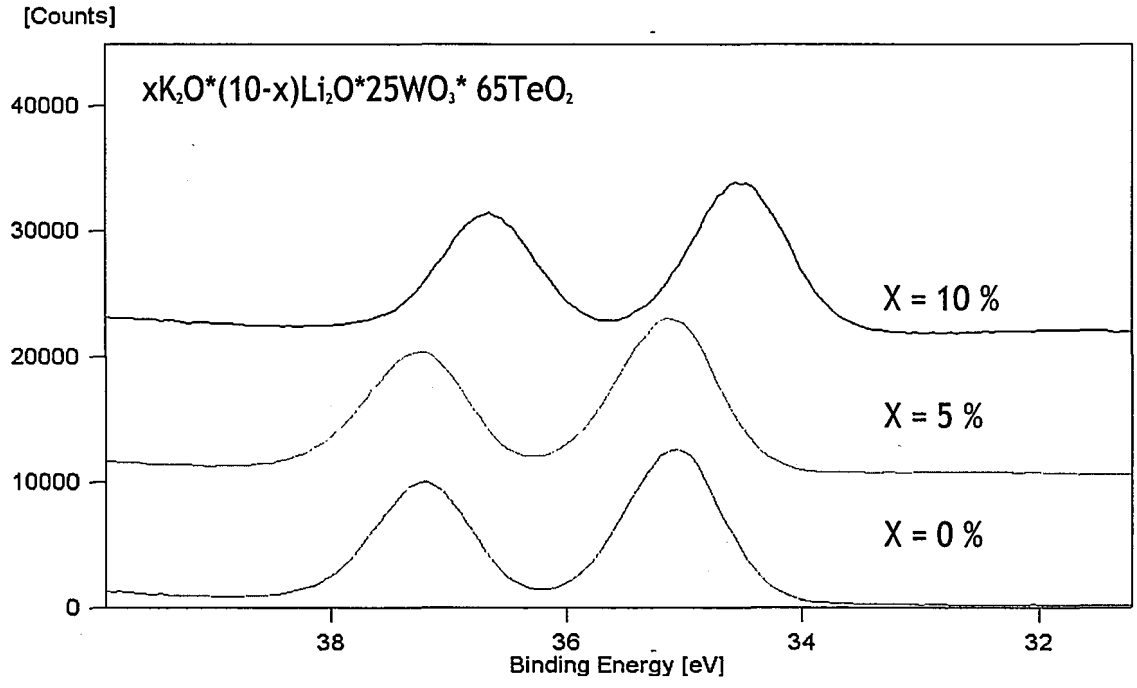

(b)

Figure 5.9. (a) O 1s (b) W 4f X-ray photoelectron spectra of $xK_2O*(10-x)Li_2O*25WO_3$ $*65TeO_2$ glass system (using Te $3d_{5/2}$ peak (576.05 eV) as internal reference).

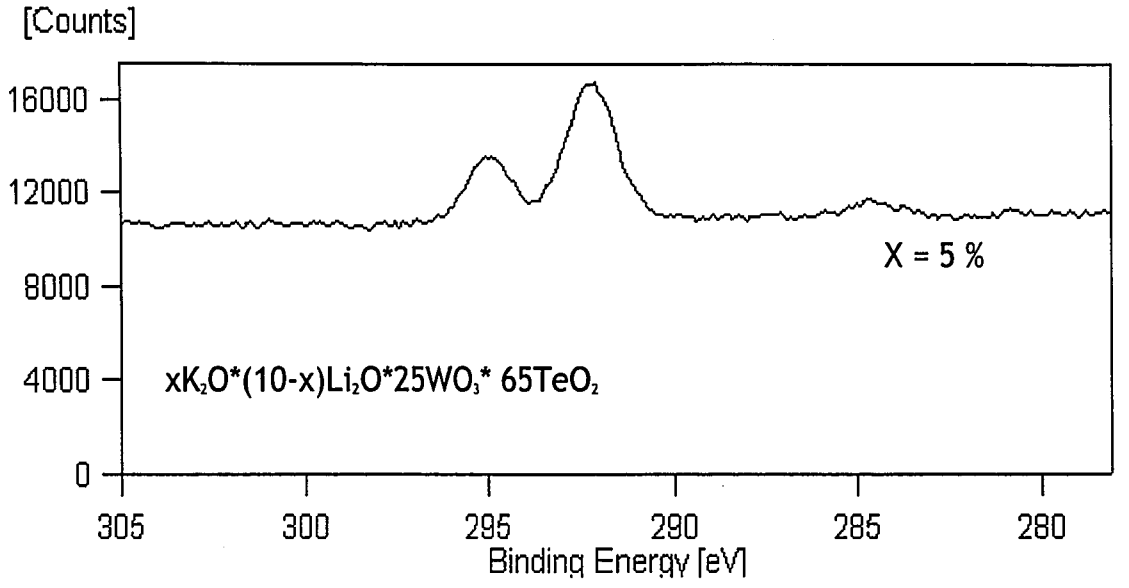

(a)

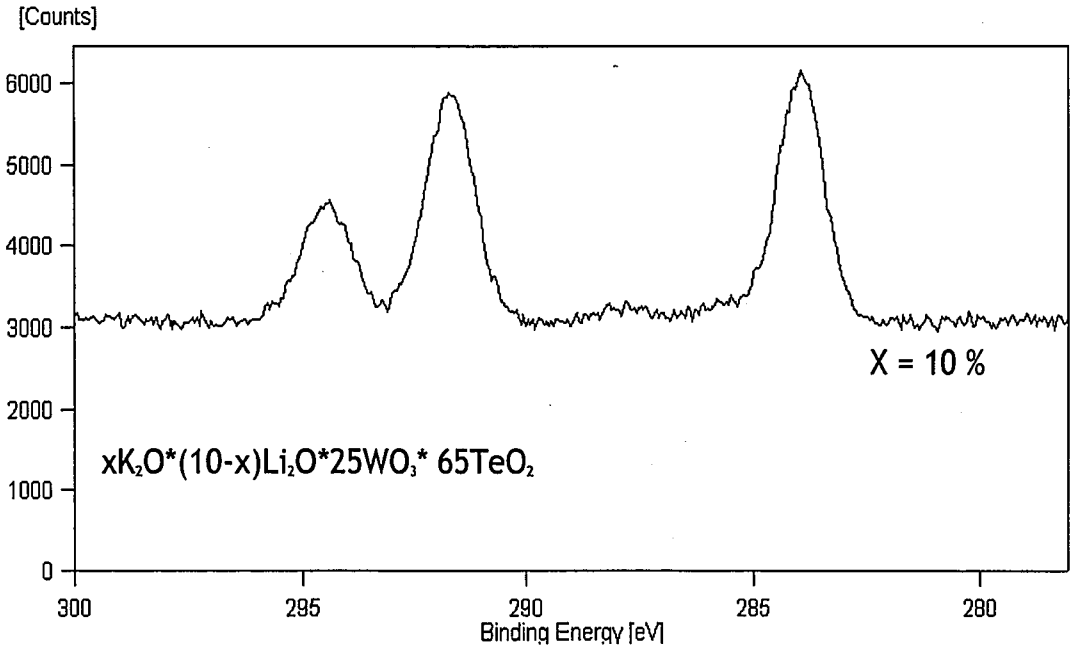

(b)

Figure 5.10. (a) 5% glass (b) 10% glass C 1s X-ray photoelectron spectra of $xK_2O*(10-x)Li_2O*25WO_3*65TeO_2$ glass system.

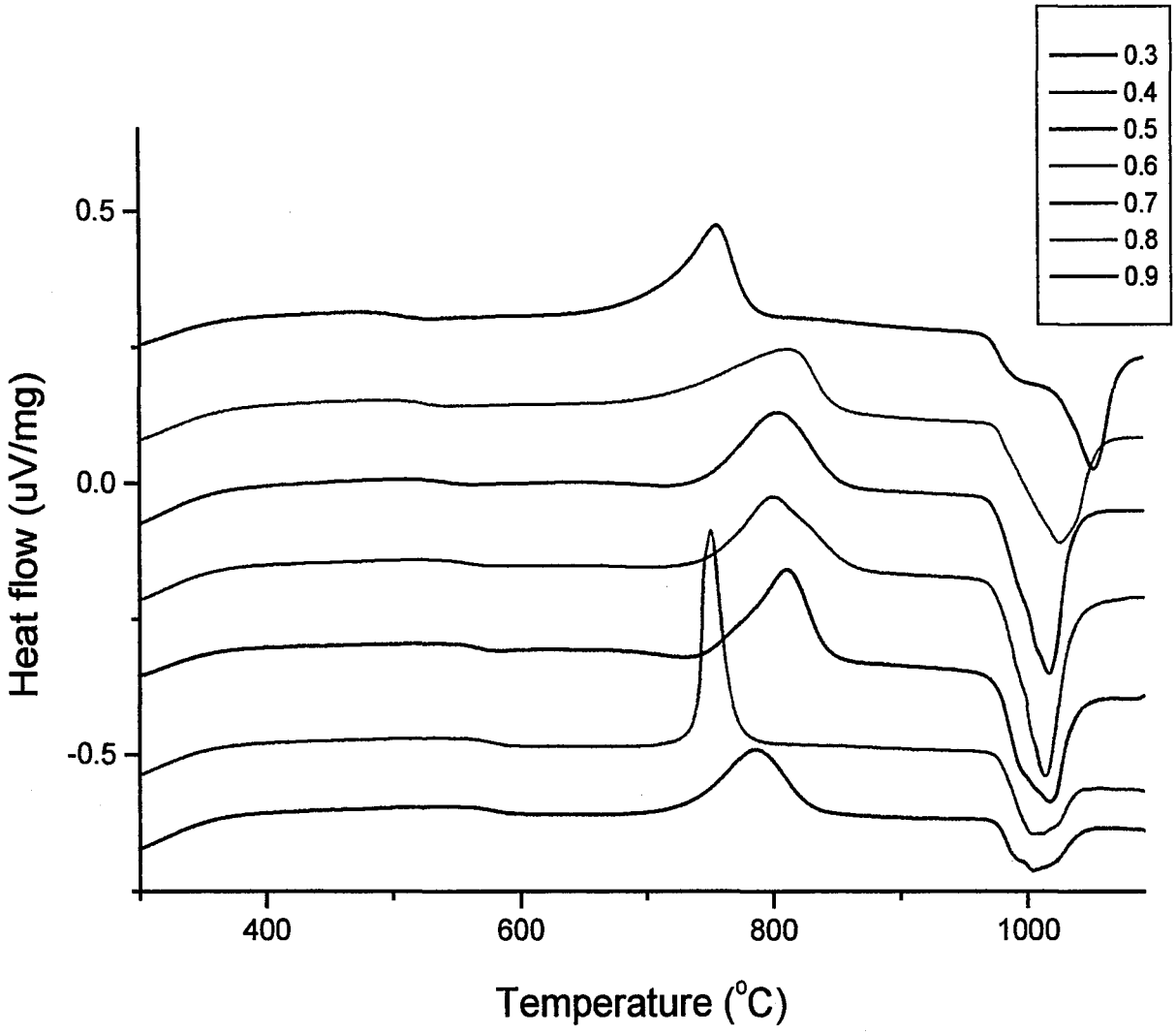

Figure 5.11. DTA curve of bulk samples of the (1+x)/2 Li_2O + (1-x)/2 Nb_2O_5 + 2x SiO_2 (x= 0.3-0.9) glass system.

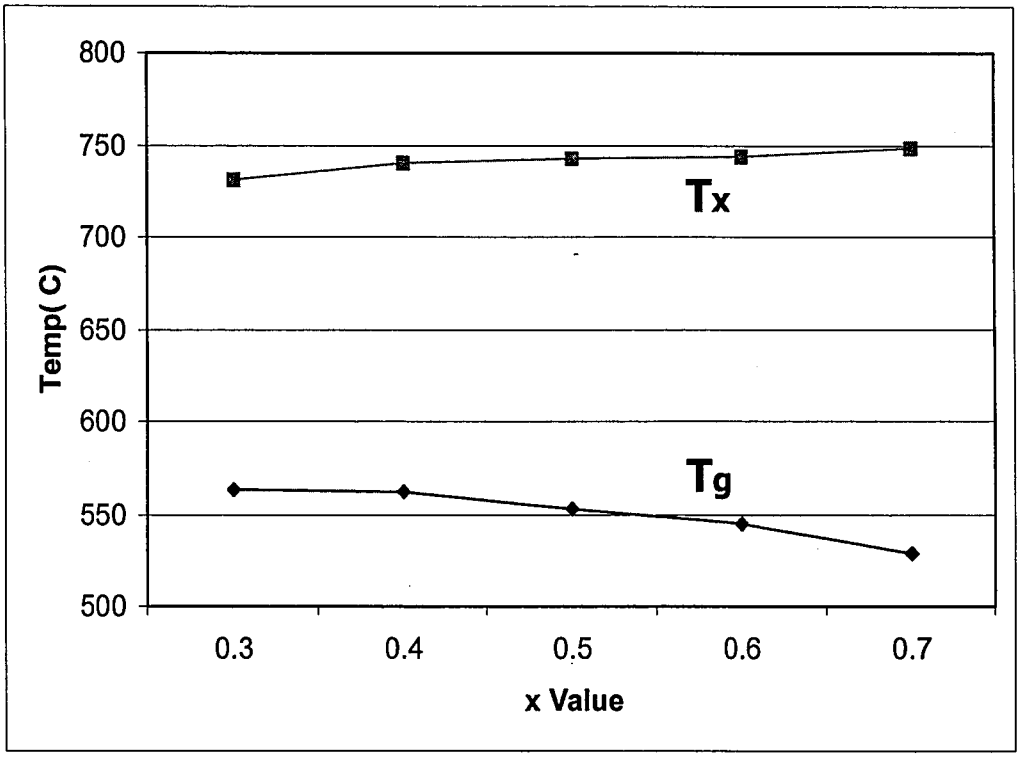

Figure 5.12. The values of Tg and Tx for (1+x)/2 Li_2O + (1-x)/2 Nb_2O_5 + 2x SiO_2 (x= 0.3-0.9) glass sample as a function of x value.

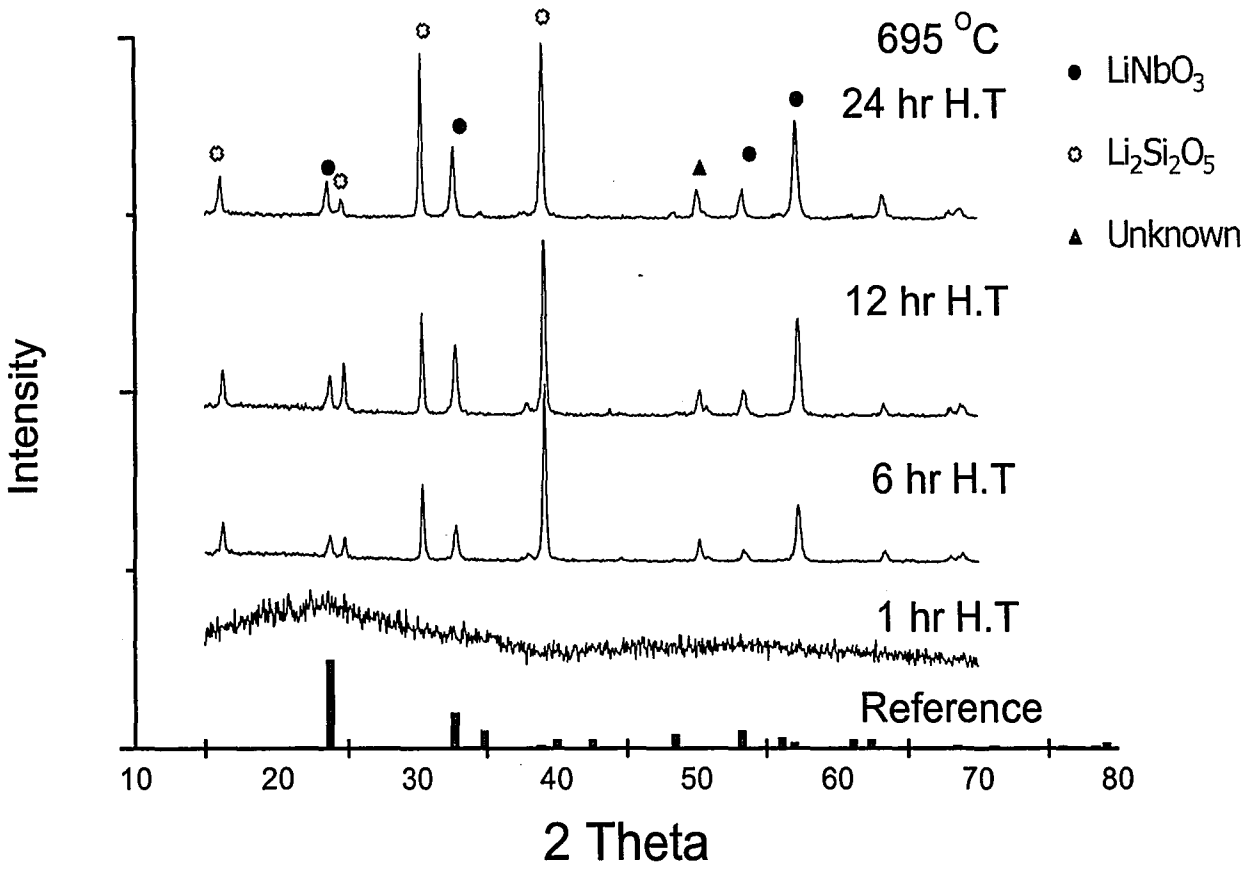

Figure 5.13. X-ray diffraction data for the sample containing 50 % of lithium niobate and 50% of lithium disilicate (x = 0.5) with different heat treatment time.

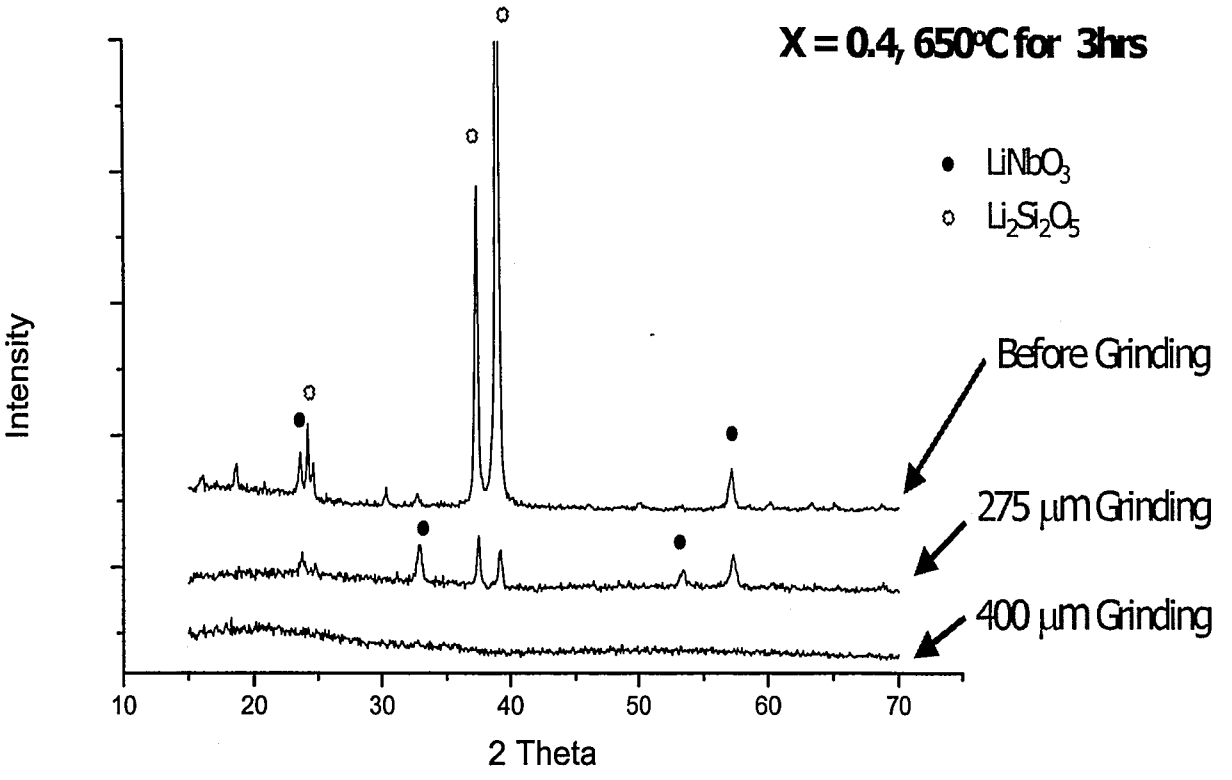

Figure 5.14. X-ray diffraction data for the 60 % lithium niobate and 40 % lithium disilicate glass heat-treated at 650 °C for 3 hours.

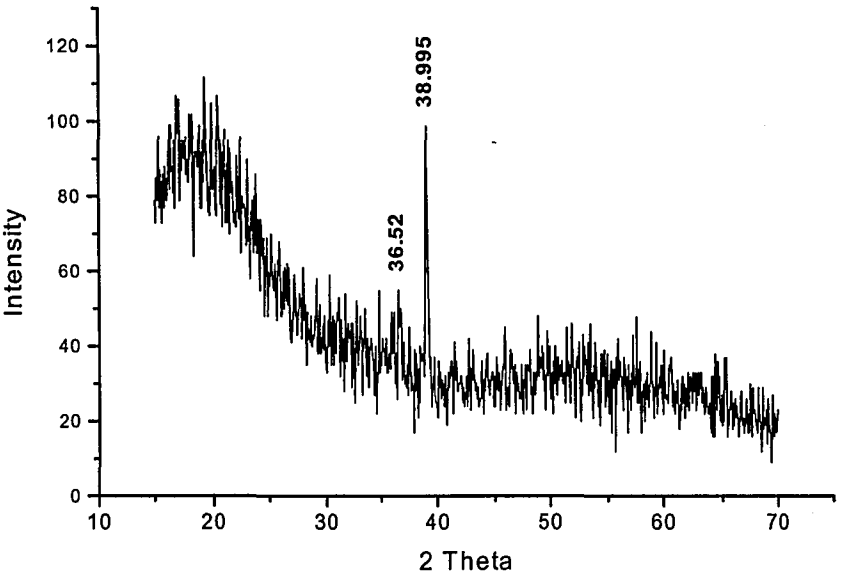

(a)

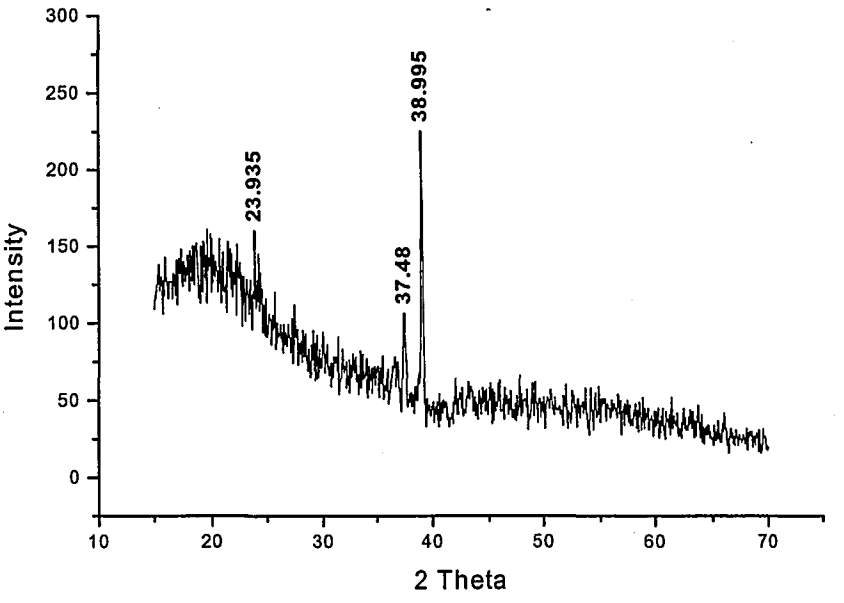

(b)

Figure 5.15. XRD pattern for (a) the heat-treated sample without electric field and (b) for the $(1+x)/2\ Li_2O + (1-x)/2\ Nb_2O_5 + 2x\ SiO_2$ (x= 0.4) sample heat-treated with electric poling.

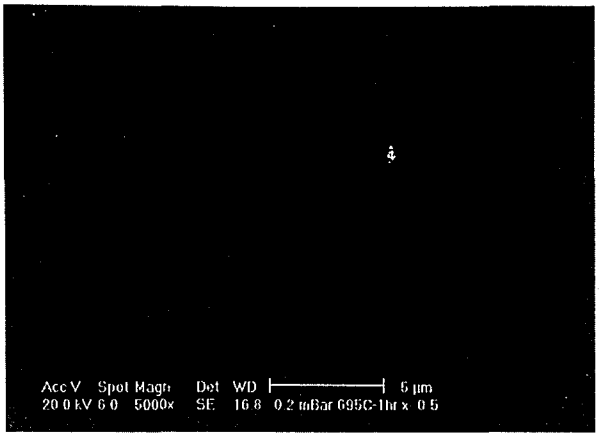

(a) 1 hour

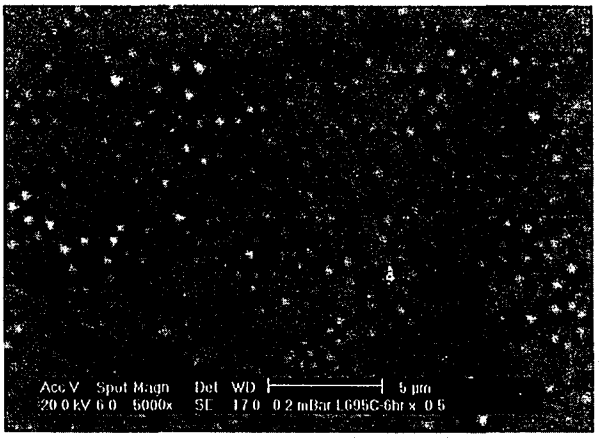

(b) 6 hours

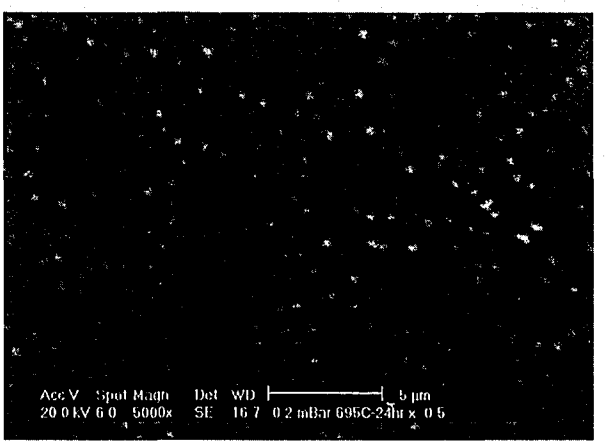

(c) 24 hours

Figure 5.16. Scanning electron microscope (SEM) image after etching: Heat-treated at 695 °C (a) 1 hour (b) 6 hour (c) 24 hours with x = 0.5 sample. Figure (b) and (c) show nano-sized crystallites.

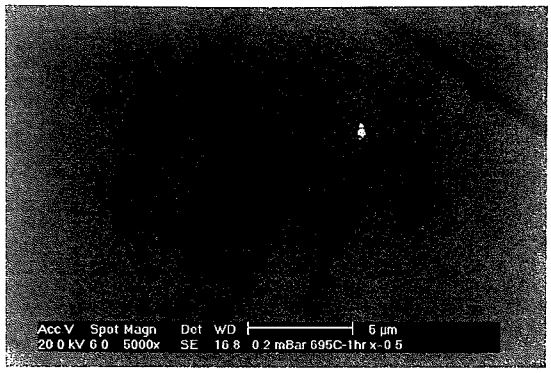

(a) 1 hour

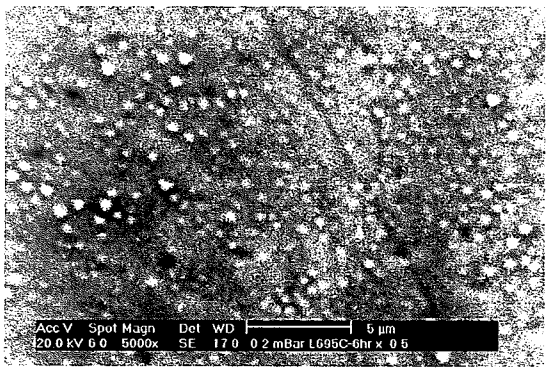

(b) 6 hours

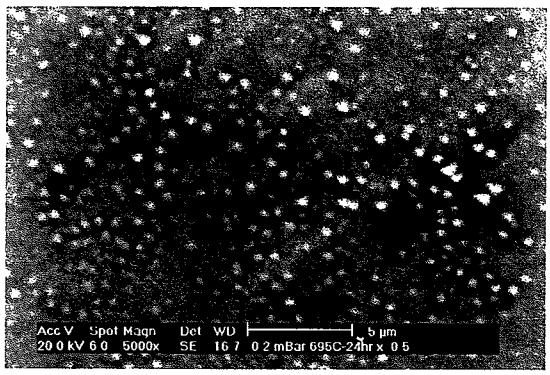

(c) 24 hours

Figure 5.16. Scanning electron microscope (SEM) image after etching: Heat-treated at 695 ^{0}C (a) 1 hour (b) 6 hour (c) 24 hours with x = 0.5 sample. Figure (b) and (c) show nano-sized crystallites.

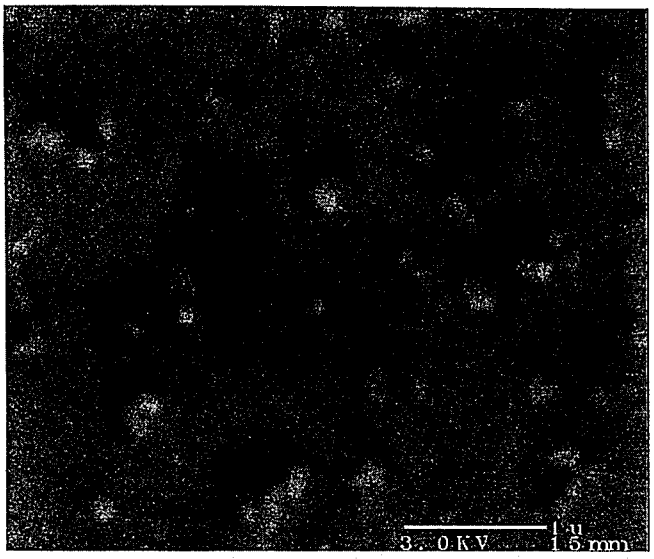

(a)

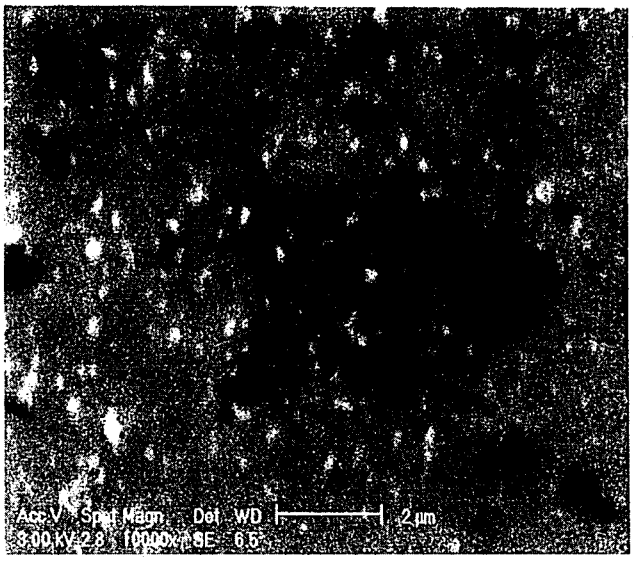

(b)

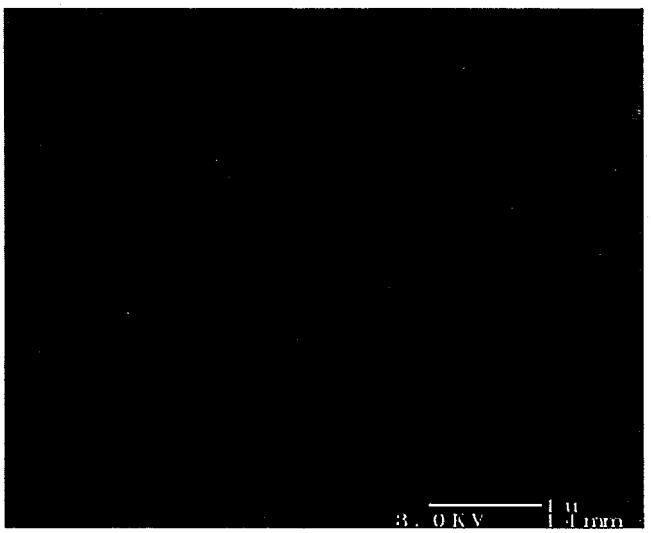

(c)

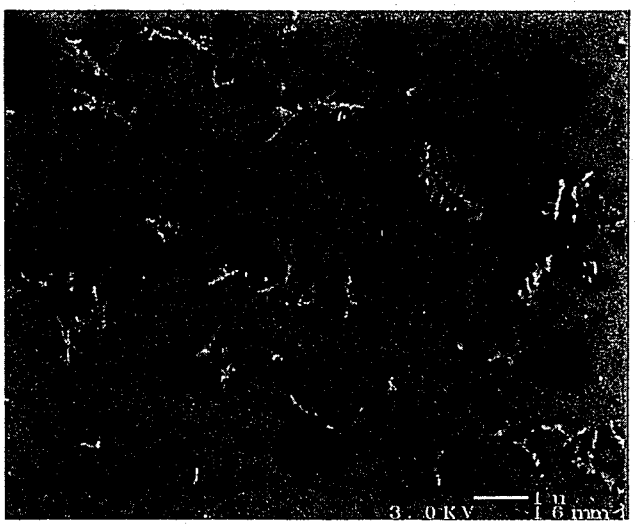

(d)

Figure 5.17. Scanning electron microscope (SEM) image of heat-treated x= 0.4 sample at 560°C for 12 hrs; (a) and (b) without applying electric field, (c) and (d) with electric field.

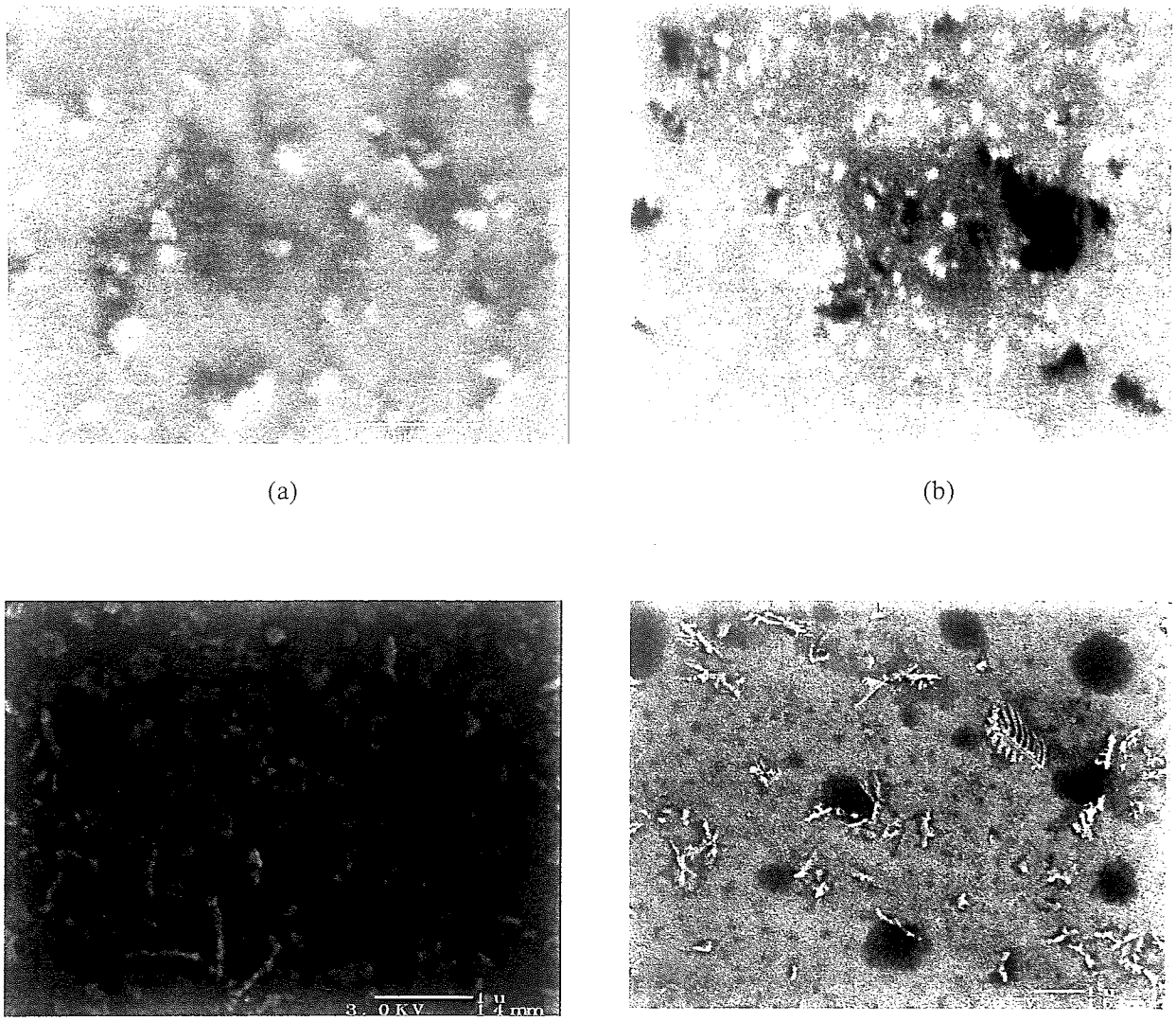

(a) (b)

(c) (d)

Figure 5.17. Scanning electron microscope (SEM) image of heat-treated x= 0.4 sample at 560°C for 12 hrs; (a) and (b) without applying electric field, (c) and (d) with electric field.

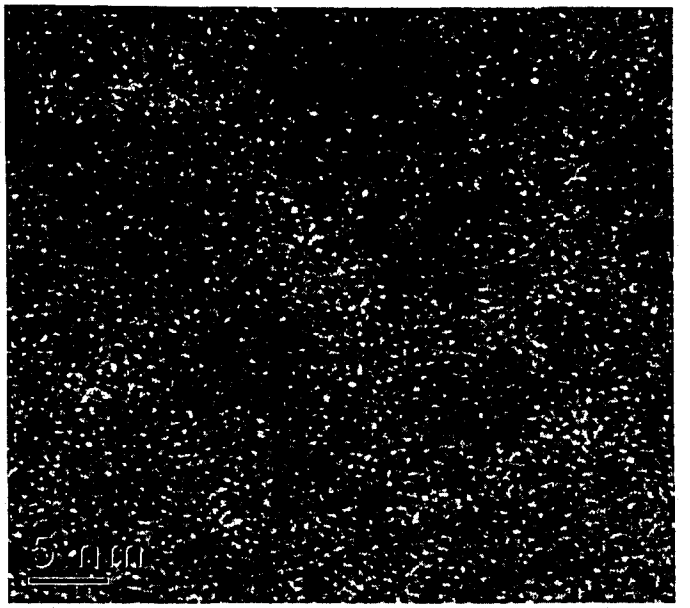

(a)

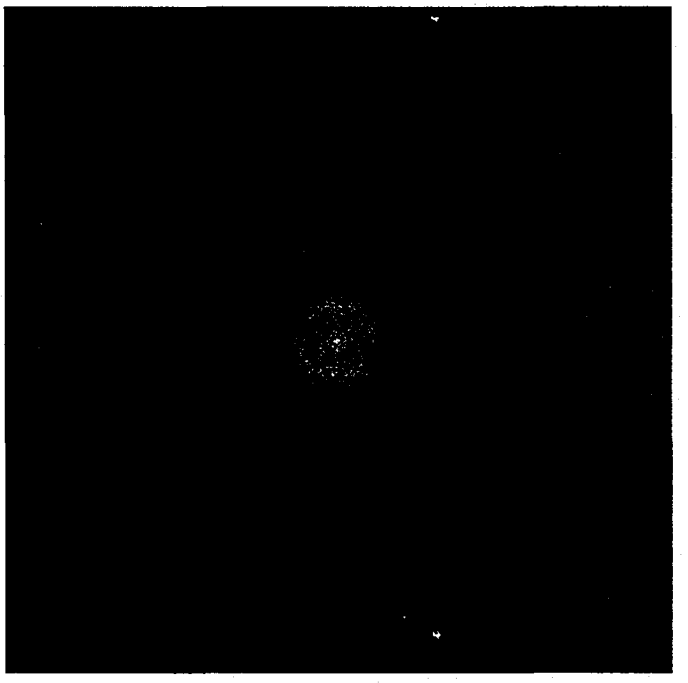

(b)

Figure 5.18. Transmission electron microscopy image from the center (a) sample image on the grid (b) sample diffraction pattern (FTT).

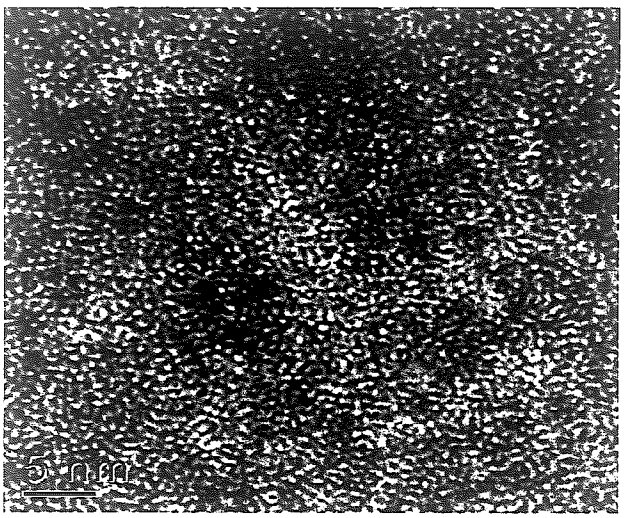

(a)

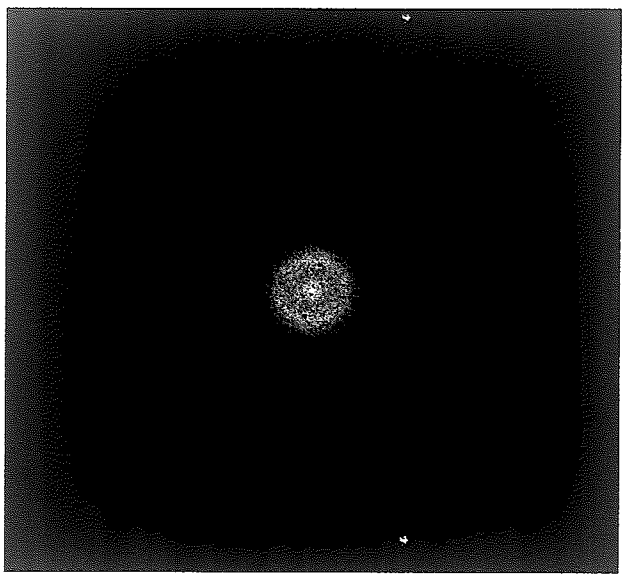

(b)

Figure 5.18. Transmission electron microscopy image from the center (a) sample image on the grid (b) sample diffraction pattern (FTT).

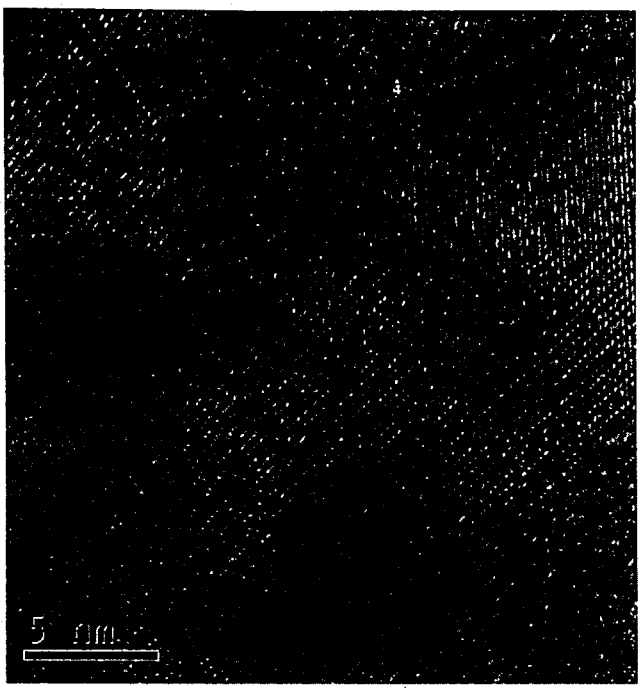

(a)

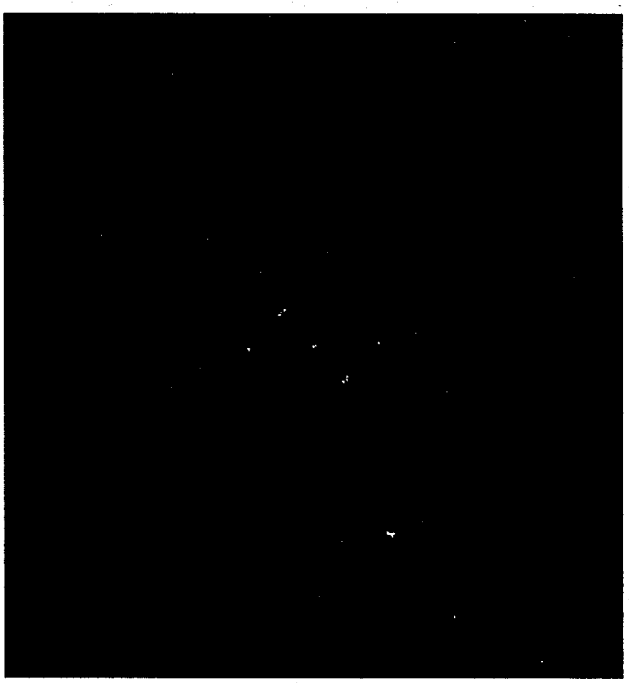

(b)

Figure 5.19. Transmission electron microscopy image from the surface (a) sample image on the grid (b) sample diffraction pattern (FTT).

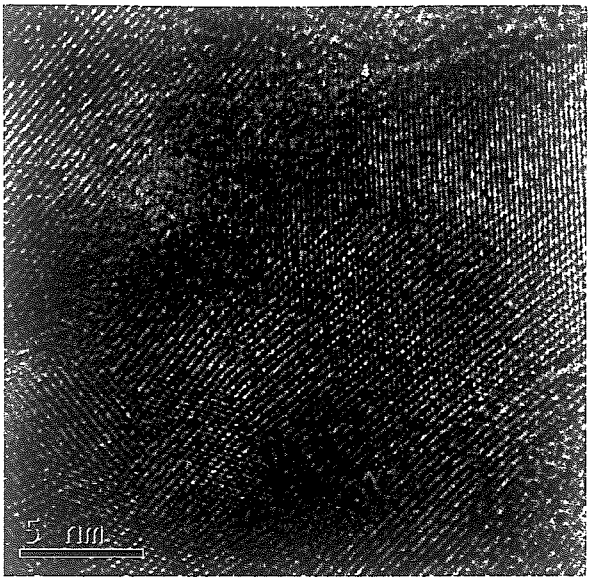

(a)

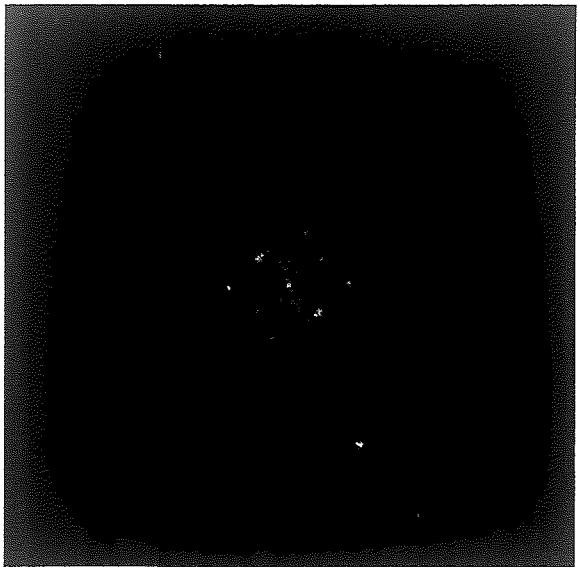

(b)

Figure 5.19. Transmission electron microscopy image from the surface (a) sample image on the grid (b) sample diffraction pattern (FTT).

Chapter 6 Discussion

6.1 Structure of tellurite glasses

6.1.1. Core Level Photoelectron Spectra of Lithium Tungsten Tellurite Glasses

When the O 1s spectra are analyzed, we find a single symmetric peak. The lack of a shoulder at high binding energy in Figure 5.2, such as reported by Himei *et al.*[25], indicate that our data for the freshly fractured surface are free from contamination from ambient. The same is also evident in the C 1s spectrum of the samples (Figure 6.1), which is a single component peak due to hydrocarbon layer deposited from the high vacuum system. We have used this C 1s peak as an internal reference at 284.6 eV. If there were contamination on the fractured glass surface, there would have been more than one peak in the C 1s photoelectron spectrum like in Figure 6.2 [25] by Himei *et al.* who found a shoulder on the high binding energy side of O 1s main peak in the sample surface exposed to air.

In Figure 5.2, only a single, symmetric Voigt (Gaussian- Lorentzian) peak is observed in the O1s photoelectron spectra and there is no variation of the shape with composition. For alkali silicate glasses, two components attributed to bridging oxygen (BO) and nonbridging oxygen (NBO) are generally observed [45, 46]. The nonbridging oxygen atoms are detected as a shoulder at the lower binding energy side of the main O 1s peak due to bridging oxygen. This is the so-called chemical shift that depends directly on the electron density of the atoms; the higher electron density around an atom results in

a lower binding energy of the ejected photoelectrons [5]. The O 1s binding energy for alkali tellurite glasses is smaller than the O 1s binding energy for the BO or NBO in alkali silicate glasses (e.g. 531.76 and 529.76 eV, respectively, for $20Na_2O*\ 80SiO_2$ glass). This implies that the electron density on the oxide ions in tellurite glasses is higher than in silicates. In general, for alkali tellurite glasses such as Li_2O-TeO_2, two components exist in the O 1s spectra. Sekiya *et al.* [8] proposed through Raman spectroscopic studies that NBOs, which are a part of the TeO_{3+1}^- polyhedra and TeO_3 trigonal pyramid (tp) units, were formed in alkali tellurite glass system due to the addition of alkali oxides. Thus the Tg decreases with the addition of Li_2O in the Li_2O-TeO_2 system due to cleavage of the network formed by TeO_4 tbp units and the consequent increase of NBOs. However, there is no nonbridging oxygen indicated in our O1s peak, indicating a more homogeneous electron distribution on the addition of WO_3.

The Te 3d photoelectron spectra in Figure 5.5 also consist of a single and symmetric Voigt peak. The shape does not change with composition, but the binding energy shifts to higher value (see Figure 5.6). Sekiya *et al.* [8] proposed that TeO_4 trigonal bipyramids (tbp) are deformed into lower-symmetry TeO_{3+1}^- polyhedra with the addition of alkali oxide. Then TeO_3 trigonal pyramids (tp) start to appear at higher alkali content. Moawad et al. [47] also have observed a variety of Te-O units in vanadium tellurite glasses. However, there is no indication of any corresponding minor components in the Te 3d photoelectron spectra of our samples.

The binding energy of the W $4f_{7/2}$ peak in Figure 5.7 also shifts in a similar manner to the O 1s and Te 3d core level peaks. Table 5.1 shows the FWHM for the O 1s,

Te $3d_{5/2}$, and W $4f_{7/2}$ core level peaks for the glass samples. There is no significant change with increasing WO_3 content and there is no other peak on the lower binding energy side in the W 4f spectra. Thus, it appears that the alkali concentration is too small to affect the core level binding energy, and WO_3 does not affect the structure significantly. Furthermore, we note that the entire W is in the + 6 oxidation state. This suggestion is supported by the XPS data for WO_3 powder [48, 49] and thin film[50], the W $4f_{7/2}$ (= 35.5 eV) and W $4f_{5/2}$ (= 37.6 eV) binding energies are very close to our data. Overall, there is little change in the core level spectra of the $10Li_2O$* xWO_3*(90-x) TeO_2 glass series with varying x.

6.1.2. Core Level Photoelectron Spectra of Mixed Alkali (Li, K) Tungsten Tellurite Glass Series

The core level peaks of the xK_2O*(10-x) Li_2O*$25WO_3$*$65TeO_2$ glass system shift toward smaller binding energy with the replacement of lithium by potassium, as shown in Figure 5.9. As the electron affinity of K is lower than that of Li, more charge is transferred from the former to the oxygen in the network. However, mixed alkali glass (5 % K_2O*5 % Li_2O) does not follow the linear trend of peak shift.

6.1.3. Valence Band Spectra

The valence band spectra for the $10Li_2O$* xWO_3*(90-x) TeO_2 glasses are shown in Figure 5.8. Relatively large changes are observed between 1 and 15 eV with increasing WO_3 content. Note that the peaks at binding energy of 13 eV and 3.5 eV

become smaller with increasing x as shown in Figure 6.3. A complex change in bonding is observed at ~ 6.8 eV. For the 15 % WO_3 sample, a peak appeared and it became broader in Figure 6.3. Then the intensity of the peak at ~ 6.8 eV increased as the composition reached 25 % WO_3.

According to Suehare et al. [20, 21] who calculated the valence band of α-TeO_2 single crystal (Figure 6.3), the peak at ~ 22 eV is mainly due to O 2s orbital with a small contribution from the Te 5s and Te 5p orbitals. The band at ~ 13 eV represents the Te 5s orbital admixed with O 2s antibonding states. The band at ~ 8 eV refers to the bonding orbitals between Te 5p and O 2p containing a small amount of O 2s antibonding character. The band at ~ 3 eV mainly originates from the O 2p states. In the XPS study of WO_3 powder [48, 49] and thin film[50], the valence band spectra show a peak at ~ 6.8 eV, which has its origin in the O 2p electron orbital. These peak assignments are compared with the valence band spectra of our compositions wherein hybridization of bonding orbitals with the addition of tungsten oxide is likely. First of all, there is no change at 22.5 eV, suggesting that O 2s does not participate in bonding with W. The intensity of the peak at ~ 13 eV in Figure 6.3 decreases on replacing TeO_2 by WO_3. Therefore, this band should be primarily due to Te 5s electrons. The band at ~ 6.8 eV, which becomes stronger with increasing WO_3, is most likely due to O 2p associated with W, which is consistent with the literature data for the valence band of WO_3 [48-50]. The peak at ~ 3.5 eV decreases sharply for x > 10 % and becomes a part of the background for the 25 % WO_3 sample. This band should be related to O 2p level associated with Te because it decreases with the addition of WO_3. The patterns at ~ 3.5 eV and 6.8 eV are reversed for

glasses with more than 15 % WO_3. From this data, it is quite apparent that tungsten affects the valence band structure of the alkali tellurite glass system.

6.1.4. Glass Transition Temperature

As determined from the thermal analysis of $10Li_2O*xWO_3*(90-x)\ TeO_2$ glass samples, the glass transition temperature increased monotonically with increasing WO_3 concentration as shown in Figure 5.1. The glass structure consists of a continuous network mainly of TeO_4 tbps at the low percent of WO_3. The increase of Tg is due to the formation of W-O-Te linkages with the increase in WO_3 content[26].

6.2 Ferroelectric Glass ceramics

6.2.1. Surface crystallization

There are two kinds of crystallization of a glass. One is bulk crystallization and the other is surface crystallization. Our hope was to obtain transparent crystallites not only on the surface but also in bulk of glass ceramics. X- ray diffraction technique was used to identify the crystallite phases. The sample that had 50 % lithium niobate and 50 % lithium disilicate showed different phases on the sample surface (Figure 5.13). Lithium disilicate and lithium niobate were present together. Simple comparison of peak intensities suggests that lithium disilicate was the majority phase but due to non-random orientation of crystallites, it was difficult to determine their relative fraction (Figure 5.13). The diffraction pattern does not differentiate between surface and bulk

crystallization, and the sample was not transparent enough to know the extent of surface crystallization from visual examination.

To increase the fraction of lithium niobate phase, 60 % of lithium niobate and 40 % of lithium disilicate sample was studied. It was heat treated at 650 °C for 3 hours. The sample was translucent and had yellow color. The XRD patterns, in Figure 5.14, show that there were both lithium niobate and lithium disilicate phases. Next, the surface was ground about 275 μm to make smooth surface and then XRD pattern was obtained. The latter XRD pattern shows that the intensity of the peaks decreased significantly. The sample was ground 125 μm (totally 400 μm) further more from the surface and the bottom pattern shows that no peak exists for this sample. It means that there was no crystallite phase present on the surface after grinding 400 μm, implying and it proved that our sample was primarily surface crystallized.

After XRD experiment, scanning electron microscope (SEM) was used to identify the crystallite phases. As shown in Figure 5.17, the nano size crystallites were observed on the surface. The 60 % of lithium niobate and 40 % of lithium disilicate sample, which was subjected to electric field during heat treatment, shows dendritic crystallization (Figure 5.17 (c) and (d)). On the other hand, the sample heat treated without electric field shows crystallites which are separate from each other (Figure 5.17 (a) and (b)). From SEM, nano-sized crystallites were observed on the surface through heat treatment. However, it was difficult to identify these crystallites because of their small size. It was also difficult to determine whether crystallites were observed on the surface or in the bulk from SEM results.

A powdered sample was studied with transmission electron microscopy (TEM) to learn more details and whether there were still nano-scale crystallites that could not be detected by SEM. First, the TEM sample was taken from the center of heat-treated 60 % lithium niobate + 40 % lithium disilicate sample. The high-resolution images (HRTEM) of the as prepared glass in Figure 5.18(a) showed that there were no crystallites and the bulk of the sample was only a glass. There is no diffraction pattern for the sample. The FFT in Figure 5.18 (b) shows the electron diffraction containing only a diffused ring. There are no spots or sharp rings. On the other hand, Figure 5.19 shows HRTEM images of the heat-treated sample surface. Figure 5.19 (a) exhibits some presence of crystallites. Figure 5.19 (b) displays the FFT of crystallite spot and non-symmetric spots are characteristics of inhomogeneous polycrystalline materials. However, it is difficult to identify the phases that exist in the sample. Overall, the nano-size crystallites are present in the surface region, but not in the bulk.

6.2.2 Effect of electric field on devitrification

The purpose of applying electric field was to prepare a glass-ceramics with oriented crystallines. The microstructure shows difference between the samples, which were devitrified with and without the applied electric field. Figure 5.17 (a) and (b) show the microstructure of glass-ceramics without any field. Less than 1 μm size crystallites were observed on the surface. Figure 5.17 (c) and (d) show different orientation of crystallites on the sample that were heat-treated with electric field. In this case, the crystallites appear connected with each other like branches. This dendrite crystal growth

was found on the surface of a transparent sample that was composed of 60 % lithium niobate and 40 % lithium disilicate and heated at 560 °C for 12 hours. The X-ray diffraction data are shown in Figure 5.15. The crystalline phases are not identified inequivocally because under these conditions, more than one crystalline phases have appeared. For the most part, in this XRD pattern, peaks may be assigned to lithium niobate and lithium disilicate phases. Transmission electron microscopy was used to analyze the crystallite phase in this sample as shown in Figure 5.19. Even though the image of crystallite was observed, we could not establish the nature of crystallites.

In conclusion, we have observed significant effect of electric field on the microstructure of the glass-ceramics, but clear evidence of alignment of crystallites is still lacking. More detailed observations are needed to identify the crystallites.

6.2.3 Structure of $x(Li_2O*2SiO_2) + (1-x)\ LiNbO_3$ glass system

The radius ratio of the cation and the neighboring oxygen anion, predicts six fold coordination for the niobium ion and four fold coordination for silicon ion [12]. Silicon ion has higher field strength due to its smaller size. Adding niobium oxide will eliminate nonbridging oxygen from the structure of these glasses. A six fold coordinated niobium ion requires a lithium ion in order to balance the $[NbO_6]^-$ unit charge. In theory, replacement of a mole of silica with a mole of niobium oxide eliminates two non-bridging oxygen from the structure and may introduce a maximum of four bridging oxygen [12]. The replacement of a single mole of lithium oxide with a mole of niobium oxide results in a net gain of three bridging oxygen and the elimination of two

nonbridging oxygen per $[NbO_6]^-$ octahedra. Therefore, niobium oxide removes nonbridging oxygen associated with the presence of alkali ions from the glass structure and it is clearly shown in the glass transition temperature, which increases with the addition of niobium oxide (see Table 4.2).

6.2.4 SHG optical property of $0.4(Li_2O*2SiO_2) + 0.6\ LiNbO_3$ glass-ceramic

As shown in Table 5.2, $0.4(Li_2O*2SiO_2) + 0.6\ LiNbO_3$ heat-treated samples have produced SHG signal even though the SHG signal measured varied quite a bit on the same sample at different points. It shows that sample is not homogeneously crystallized on the surface and, as shown in SEM image, the crystallites are irregularly oriented on the surface. In addition, there is no evidence that electric field aligns the crystallites.

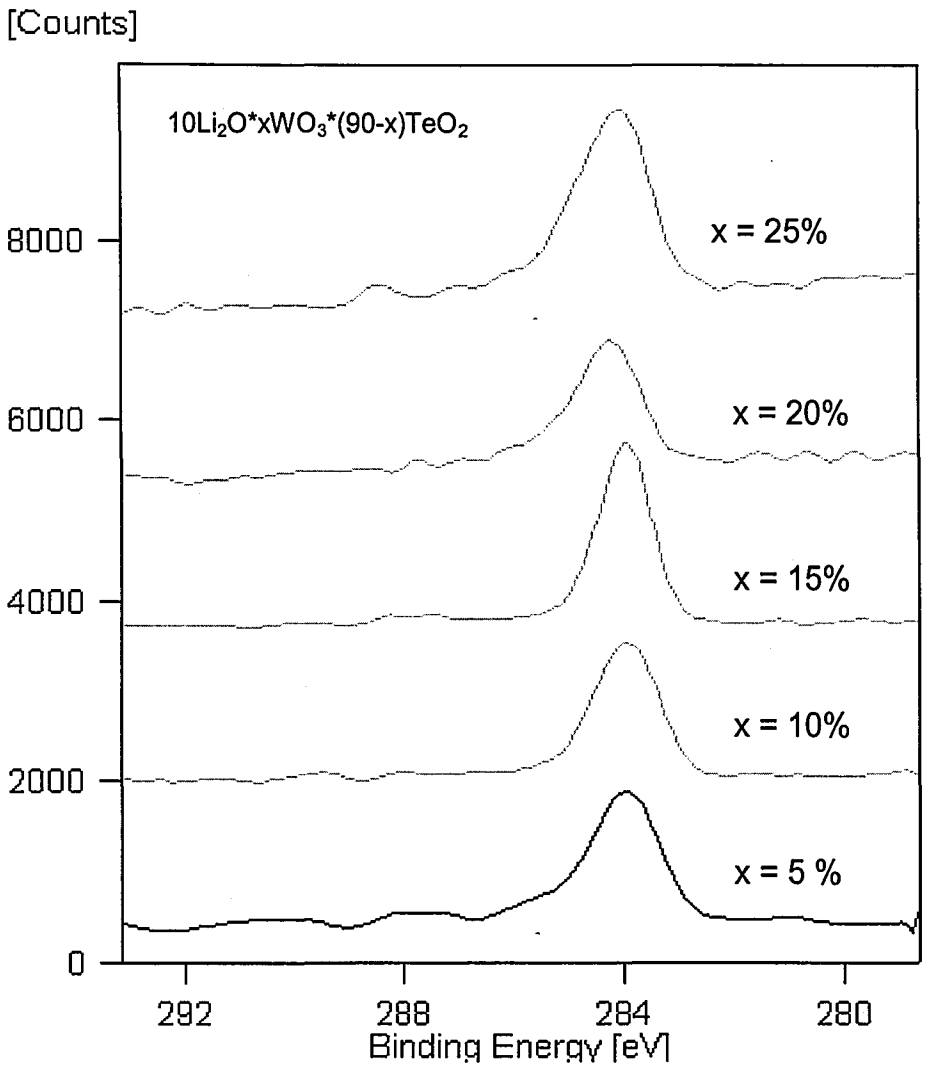

Figure 6.1. C1s X-ray photoelectron spectra for the glass fractured in a vacuum for each composition.

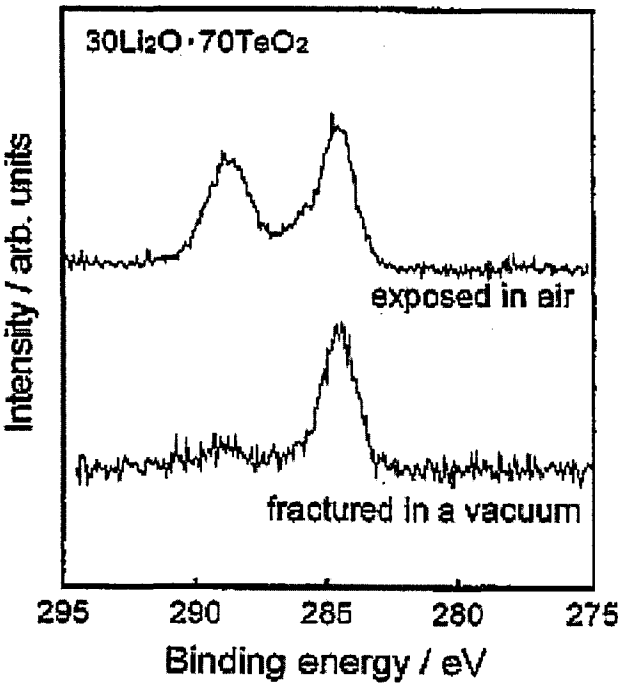

Figure 6.2. C1s X-ray photoelectron spectra for the surface exposed in air and that for the surface fractured in a vacuum for 30 Li_2O *70 TeO_2 glass [25].

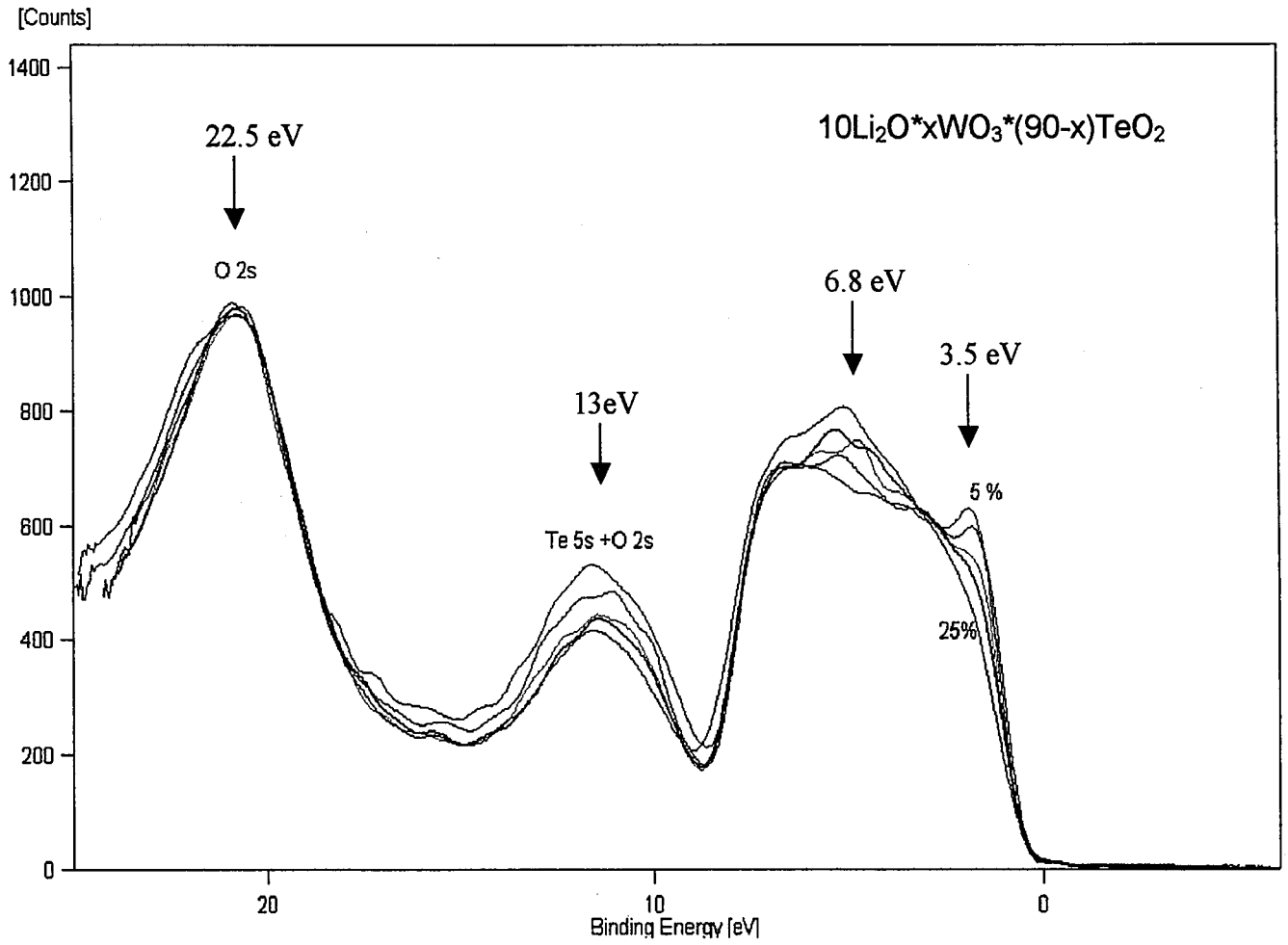

Figure 6.3. X-ray photoelectron spectrum near the valence band in $10Li_2O*xWO_3*(90-x)TeO_2$ glass system are compared and indicated binding energies are calculated by Suehare et al.[20, 21].

Chapter 7 Conclusions

The shape of core-level XPS spectrum for all the elements show little change as TeO_2 is replaced by WO_3 in the $10Li_2O*xWO_3*(90-x)$ TeO_2 glass series. Thus WO_3 behaves as a network former. The W-O-Te linkages are stronger than the Te-O-Te linkages so that the glass transition temperature increases with x. By comparison, the valence band spectra show significant systematic changes that are consistent with the variation of composition.

For studying transparent glass-ceramics containing $LiNbO_3$, a series of x $(Li_2O*2SiO_2)$ * (1-x)$(Li_2O*Nb_2O_5)$ (mol%) glasses was prepared by the melt quench method with x = 0.3 – 0.9. $LiNbO_3$ crystallites were created by controlled heat treatment and they grew with time. This glass-ceramic containing nano size $LiNbO_3$ crystallites was transparent. Most crystallization in x $(Li_2O*2SiO_2)$ * (1-x)$(Li_2O*Nb_2O_5)$ glass system occurs on the surface, and not in the bulk, as indicated by XRD, SEM and TEM. The crystallite phases, as identified by XRD, included lithium niobate mixed with lithium disilicate. The transmission electron microscopy did not show any nano-size crystallite in the center of the sample but only on surface. For the 60 % lithium niobate and 40 % lithium disilicate glass-ceramic composition, we have observed significant effect of electric field on the microstructure of the glass-ceramics but there is no clear evidence to understand alignment of crystallites. SHG signal was observed but the sample crystallized inhomogeneously.

References

[1]D. R. Uhlmann and N. J. Kreidl, Optical Properties of Glass, American Ceramic Society, Westerville, OH, 1991.

[2] H. Nasu, T. Uchigaki, K.Kamiya, H. Janbara and K. Kubodera, Jpn. J. Appl. Phys. 31 (1992) 3899.

[3] S. H. Kim, T. Yoko, and S. Sakka, J. Am. Cerm. Soc. 76 (1993) 2486.

[4] J. S. Wang, E. M. Vogel and E. Snitzer, Opt. Mat., 3 (1996) 187.

[5] J. Heo, D. Lam, G.H. Sigel, Jr., E.A. Mendoza and D. A. Hensley, J. Am. Ceram. Soc. 75 (1992) 277.

[6] K. Suzuki, J. Non-Cryst. Solids 95-96 (1978) 15.

[7] M. Dimitrova, Y. Dimitriev, M. Arnaudov and V. Dimitrov, Phys. Chem. Galsses 30 (1989) 260.

[8] T. Sekiya, N. Mochida, A. Ohtsuka and M.Tonokawa, J. Non-Cryst. Solids 144 (1992) 128.

[9] Y. Himei, A. Osaka, T. Nanba, and Y. Miura, J. Non-Cryst. Solids 177 (1994) 164.

[10] D. C. Boyd, P.S. Danielson, and D.A.Thompson, Kirk-Othmer Encyclopedia of Chemical Technology, 4th ed, Vol 12, John Wiley & Sons, Inc. (1994).

[11] M. M. Abouelleil and F.J. Leonberger, J. Am. Ceram. Soc. 72 (1989) 1311.

[12] D. E. Vernacotola and J. E. Shelby, Phys. Chem. Glasses, 35 (1994) 153.

[13] P. Pernice, A. Aronne, V. N. Sigaev, P. D. Sarkisov, V. I. Molev, and S. Y. Stefanovich, J. Am. Ceram. Soc. 82 (1999) 3447.

[14] C. Hirayama and D. Berg, J. Am. Ceram. Soc. 46 (1963) 85.

[15] M. M Layton and A. Herczog, J. Am. Ceram. Soc. 50 (7) (1967) 369.

[16] A. Herczog, J. Am. Ceram. Soc. 73 (1990) 2743.

[17] H. C. Zeng, K. Tanaka, K. Hirao, and N. Soga, J.Non-Cryst. Solids, 209 (1997) 112.

[18] K. Gerth, C. Russel, and R. Keding, Phys. Chem. Glasses, 40(3), (1999) 135.

[19] Y. Ding, Akiyoshi Osaka, and Yoshinari Miura, J. Appl. Phys. 77(5), (1995) 132.

[20] S. Suehara, K. Yamamoto, S. Hishita, and A. Nukui, Phys. Rev. B, Vol. 50, No. 11 (1994) 7981.

[21] S. Suehara, K. Yamamoto, S. Hishita, and A. Nukui, Phys. Rev. B, Vol. 51, No. 21 (1995) 14919.

[22] V. H. Beyer, Zeitschrift fur kristallographie, Vol. 124 (1967) 228.

[23] A. V. Johnson, C. Wright, and A. Yarker, J. Non Cryst. Solids, Vol. 81 (1986) 163.

[24] W. Margulis, F. C. Garcia, E. N. Hering, L. C. Guedes Valente, B. Lesche, F. Laurell, and I. C. S. Carvalho, MRS Bulletin 23 (1998) 31.

[25] Y. Himei, Y. Miura, T. Nanba, and A. Osaka, J. Non-Cryst. Solids 211 (1997) 64.

[26] T. Sekiya, N. Mochida, S. Ogawa, J. Non-Cryst. Solids 176 (1994) 105.

[27] S. Neov, V. Kozhukhzrov, I. Gerasimova, K. Krezhov, and B. Sidzhimov, J. Phys. C: Solid State Phys, Vol. 12 (1979) 2475.

[28] A. Yakhkind, J. Amer. Ceram, Soc., 49 (1966) 670.

[29] V. Dimitrov, M. Awnaudou, and Y. Dimitriev, Monatsh. Chem. 115 (1984) 987.

[30] Y. Dimitriev, V. Dimitrov, E. Gatev, E. Kashchieva and H. Petokov, J. Non-Cryst. Solids 95&96 (1987) 937.

[31] V. Kozhukharov, S. Neov, I. Gerasimova, and R. Mikula, J. Mater. Sci. 21 (1986) 1707.

[32] G. H. Beall and D. A. Duke, J. Mater. Sci. 4 (1969) 340.

[33] G. Partridge and S. V. Phillips, Glass Technology 32 (1991) 82.

[34] N. F. Borrelli, J. Appl. Phys. 61 (1987) 5399.

[35] N. F. Borrelli, J. Appl. Phys. 38 (1967) 4243.

[36] A. Herczog, J. Am. Ceram. Soc. 47 (1964) 107.

[37] N. F. Borrelli and M. M. Layton, J. Non-Cryst. Sol. 6 (1971) 197.

[38] R. A. Myers, N. Mukherjee, and S. R. J. Brueck, Opt. Lett. 16 (1991) 1732.

[39] K. Tanaka, K. Kashima, K. Hirao, N. Soga, A. Miro, and H. Nasu, J. Non-Cryst. Solids 185 (1995) 123.

[40] Y. Takahashi, Y. Benino, V.V. Dimitrov, and T. Komatsu, Phys. Chem. Glasses. 41 (2000) 225.

[41] K. Tanaka, H. Kuroda, A. Narazaki, K. Hirao, and N. soga, J. Mater. Sci. Lett. 17 (1998) 1063.

[42] K. Shioya, T. Komatsu, H. G. Kim, R. Sato, and K. Matusita, J. Non-Cryst. Solids 189 (1995) 16.

[43] Natl. Bur. Stand. (U.S.) Monogr. 25, 6 (1968) 22.

[44] Kalinina, Inorg. Mater. (Engl. Transl.), 6 (1970) 796.

[45] R. Bruckner, H. U. Chun and H. Goretzki, Glastech. Ber. 51 (1978) 1.

[46] S. Matsumoto, Y. Miura, T. Nanba and A. Osaka, Proc. 17th Int. Congress on Glass, Vol 3. (1995) 72.

[47] H. M. Moawad, J. Toulouse, H. Jain, O. Latinovic and A. R. Kortan, Ceram. Trans (Optoelectronic Materials Technology in the Information Age), 126, (2002) 45.

[48] R. J. Colton and J. W. Rabalais, Inorg. Chem. 15 (1976) 236.

[49] T. H. Fleisch and G. J. Mains, J. Chem. Phys., 76 (1982) 780.

[50] R. J. Colton, A. M. Guzman and J. W. Rabalais, J. Appl. Phys. 49 (1978) 409.

Vita

Jong Wook Lim was born to Sam Rang Lim and Hwa Lee on August 2, 1972 in Seoul, Korea. He attended Young Dong High School before attending Coe College. He earned a B.S. with a major in Physics while also minoring in Mathematics from Coe College in May of 2000 before enrolling in M.S. program in Materials Science and Engineering at Lehigh University.

END OF TITLE